Stefan Humbla & Matthias A. Hein (Ed.)

Proceedings of the 17th International Student Seminar "Microwave and Optical Applications of Novel Phenomena and Technologies"

PROCEEDINGS OF THE

17th INTERNATIONAL STUDENT
SEMINAR

MICROWAVE AND OPTICAL APPLICATIONS OF NOVEL PHENOMENA AND TECHNOLOGIES

JUNE 8-10, 2010, ILMENAU, GERMANY

Edited by
Stefan Humbla & Matthias A. Hein

Universitätsverlag Ilmenau
2011

Titelfoto: photocase.com | AlexFlint

Content

Full papers

Preface

Dear Reader,

The 2010 International Student Seminar, held at Ilmenau University of Technology, was the 17th of its kind and covered a broad spectrum of topics as intended by the theme "Microwave and optical applications of novel phenomena and technologies".
The tradition started in 1994 at Chalmers University of Technology, Sweden with support of Prof. E. Kollberg. Thanks to the inspiring work and ongoing enthusiasm of Prof. Orest G. Vendik and Prof. Irina B. Vendik, the mental "parents" of the seminar series, the seminar was held seven times in St. Petersburg, Russia. Further International Student Seminars were hosted by academia in Sweden, France, Germany, UK, and Finland; eventually, we at Ilmenau are proud to belong to the hosts.
In 2010, the scope of the ISS-17 covered plasmons, metamaterials, superconductivity, as well as device, system, and technology aspects for high frequency applications. Several invited presentations delivered tutorial background knowledge of recent research activities and shared some visionary perspectives.

We would like to thank all participants for their valuable contributions and fruitful discussion, that made the 17th Student Seminar again a success.

The Seminar organizers   Stefan Humbla & Matthias Hein
                                         RF & Microwaves Research Laboratory
                                            Ilmenau University of Technology

Participants of the 17th International Student Seminar

Invited presentations

Mario Schühler
Periodically structured surfaces and their application to planar antennas

Martin Djiango
The Power of Plasmonic Resonances: Biosensors, Nanolasers, Metamaterials

Hannes Toepfer, Thomas Ortlepp
Time-Domain Analysis of Fast Phenomena in Signal Transmission Structures

Matthias Hein
Compact diversity antennas for mobile Communications

Johannes Trabert
Microwave modules system design in three dimensional LTCC technology

Stefan Humbla
Ceramic Modules for Space Applications and future developments

Miniature LTCC Wilkinson Power Dividers Using Artificial Right- and Left-handed Transmission Lines

Irina Munina, Polina Kapitanova, and Dmitry Kholodnyak

Microwave Microelectronics Laboratory, Department of Microelectronics & Radio Engineering, St. Petersburg Electrotechnical University "LETI", 5 Prof. Popov st., 197376 St. Petersburg, Russia

Abstract

Artificial quasi-lumped-element implementation of the quarter-wavelength transmission line sections results in a remarkable size reduction of the Wilkinson power divider. The multilayer Low Temperature Co-fired Ceramics (LTCC) technology suits well for a realization of microwave devices based on quasi-lumped elements that allows further miniaturization due to allocation of elements within different layers. Using a combination of conventional (right-handed) transmission lines, in which the dispersion is positive, and artificial metamaterial (left-handed) transmission lines with negative dispersion makes it possible to design Wilkinson-type power dividers providing 180° phase difference between output signals. This paper presents the design of miniature 0° and 180° Wilkinson power dividers developed for the central frequency of 3 GHz. The devices, which were implemented using the LTCC technology, are characterized by 30% operational bandwidth and have a small size. An approach to design a reconfigurable in-phase/out-of-phase Wilkinson power divider is discussed.

Keywords — left-handed transmission line (LH TL), the Wilkinson power divider, Low Temperature Co-Fired Ceramics (LTCC), lumped elements.

I.   Introduction

The Wilkinson power divider-combiner is a three-port very popular microwave device used in various RF and microwave systems. It provides matching of all the ports, low loss, high isolation, and in-phase power splitting between output ports. On the other hand, Wilkinson-type power dividers providing 180° phase difference between output signals can be designed using a combination of conventional transmission lines (TLs), in which the dispersion is positive (right-handed transmission lines – RH TLs), and artificial metamaterial TLs with negative dispersion (left-handed transmission lines – LH TLs) [1]-[3]. Such an out-of-phase divider can be employed as a balun with all ports matched.

The LH TLs can be only engineered in an artificial way using series lumped or quasi-lumped capacitors connected in series and shunt inductors. Artificial quasi-lumped-element implementation of the right-handed TLs along with the left-handed ones could result in a remarkable size reduction of the device. The multilayer Low Temperature Co-fired Ceramics (LTCC) technology is well suited for a realization of microwave devices based on quasi-lumped elements that allows further device miniaturization due to allocation of elements within different layers.

This paper presents design of miniature in-phase and out-of-phase Wilkinson power dividers based on artificial RH and LH TL sections. A concept of a broadband reconfigurable Wilkinson-type power divider is proposed.
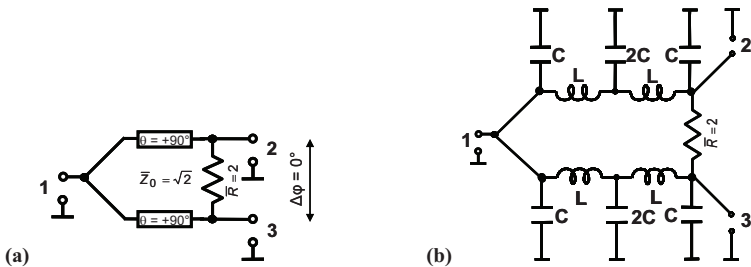

Fig. 1. Schematic diagram of the Wilkinson power divider: based on distributed TLs (a) and based on artificial RH TL sections implemented as a cascade of two Π-cells (b).

II. Design of miniature Wilkinson power dividers

The classical Wilkinson power divider consists of two quarter wavelength TLs sections and a lumped resistor, which is connected between outputs (Fig. 1-a). Employing distributed TLs leads to a large size of the divider, especially in low-frequency applications. In order to decrease the size of the device, the conventional TL sections can be realized as artificial ones based on LC-cells. Characteristics of a TL section depend strongly on the number of unit cells used per wavelength. However, using two cascaded unit cells per quarter-wavelength is enough to provide the characteristics being very close to those of an ideal TL section in the bandwidth of one octave [1]. Fig. 1-b shows an equivalent circuit of the Wilkinson power divider with each quarter-wavelength TL sections replaced by two cascaded Π-cells. Parallel-plate capacitors and stacked inductors can be used to implement such a device by means of the LTCC technology.

Fig. 2-a presents the 3D-view of the Wilkinson power divider structure, which was embedded into 8 LTCC layers of DuPont Green TapeTM 951 with $\varepsilon_r = 7.8$ and the thickness of 95 µm after co-firing. The substrate size is 8 mm × 5.5 mm that corresponds to $\lambda g/5 \times \lambda g/8$. Characteristics obtained by EM simulation are shown in Fig. 2-b in comparison with those of the Wilkinson power divider based on distributed TLs. Note, that the operational bandwidth and other electrical characteristics remained nearly the same while the size of the device was reduced.
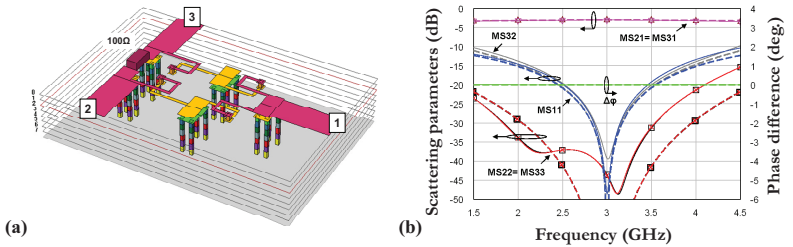

Fig. 2. Multilayer LTCC structure of the miniature Wilkinson power divider (a) and characteristics of the Wilkinson power divider based on quasi-lumped elements (solid lines) and on distributed TL sections (dashed lines) (b).
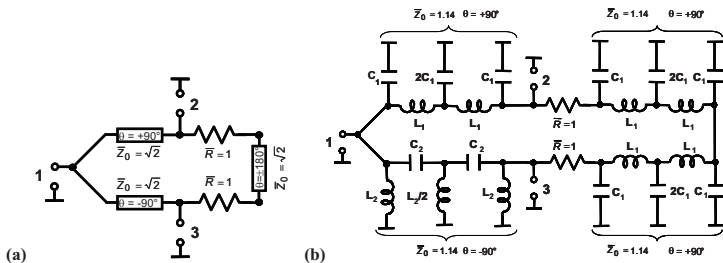
Fig. 3. Schematic diagram of the out-of-phase Wilkinson power divider: based on distributed TLs (a) and based on artificial RH TL sections implemented as two cascaded -cells (b).

Out-of-phase modifications of the Wilkinson power divider, which employ LH and RH TL sections with the electrical length of –90° and +90°, respectively, was reported in [2]-[4]. Fig. 3-a illustrates the broadband configuration of the 180° Wilkinson power divider proposed in [4].

Here we present a quasi -lumped-element realization of this power divider using the LTCC technology (Fig. 4-a). The same LTCC stack as for the above mentioned in-phase Wilkinson divider was used. The size of the out-of-phase device version is 8 mm × 10 mm ($\lambda g/5 \times \lambda g/4$). The results of EM simulation of the device characteristics are presented in Fig. 4-b.

III.   Design of broadband reconfigurable 0°/180° Wilkinson power divider

Among the band broadening techniques known for the Wilkinson power divider, a modification of the device structure by introducing a balun transformer and a dummy load [5] is of special interest, because such a transformer can be easily designed as a combination of the quarter-wavelength RH and LH TL sections with a shunt resistor between them. Using this transformer allows designing a broadband in-phase Wilkinson power divider. It is interesting to note, that this broadband divider consists of the same set of TL sections with the same values of electrical length and characteristic impedance as the rat-race ring with one terminated port (Fig. 5-a), which employs the quarter-wavelength LH TL instead of three-
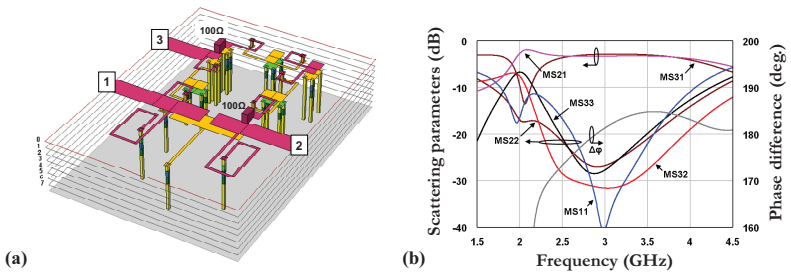
4

Fig. 4. Out-of-phase Wilkinson power divider: multilayer LTCC structure (a) and characteristics obtained by EM simulation (b).

quarter-wavelength RH TL section [6]. For more clearness, the conventional rat-race-ring is shown in Fig. 5 before replacing the electrically long RH TL section by the LH TL. In fact the same device can operate as an out-of-phase divider if another port is terminated as shown in Fig. 5-b.

Switching between the input ports and between the terminated ports corresponding to the both cases allows designing a broadband reconfigurable 0°/180° three-port power divider-combiner, which can provide output signals either in phase or out of phase. Necessary switching can be performed with the aid of a double-pole double-throw (DPDT) switch as illustrated in Fig. 5-c.

Fig. 6-a shows an equivalent circuit of the broadband rat-race ring with every quarter-wavelength RH and LH TL sections replaced by two cascaded Π-cells. It can be used as a core of the 0°/180° reconfigurable power divider. The miniature rat-race ring was accomplished on quasi-lumped elements embedded into 8 layers of 95 μm thick DuPont Green TapeTM 951 LTCC as shown in Fig. 6 b. The LTCC structure has the same size as
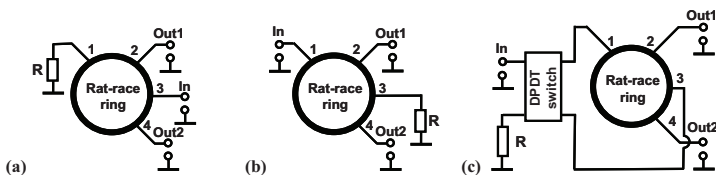
Fig. 5. Schematic diagram of the broadband 0° (a), 180° (b) and reconfigurable 0°/180° (c) Wilkinson power dividers.
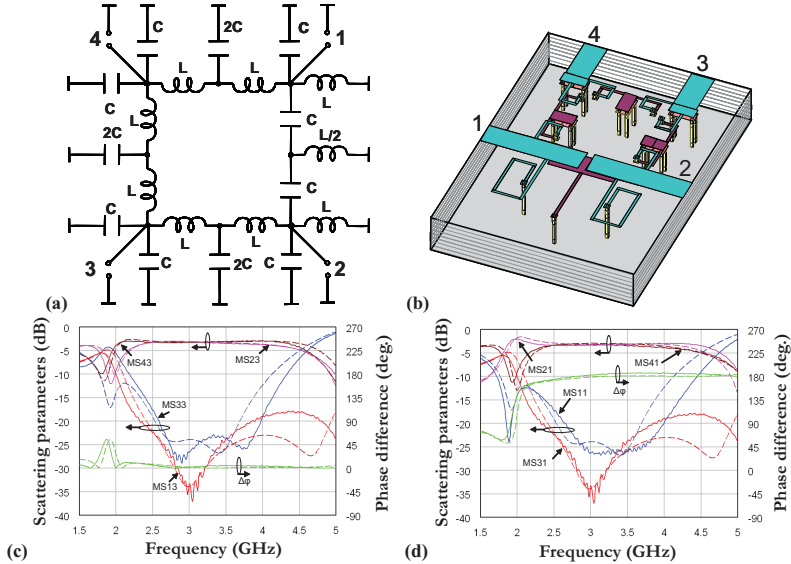
Fig. 6. Rat-race ring based on artificial LH and RH TL sections implemented as two cascaded Π-cells: equivalent circuit (a); multilayer LTCC structure (b); simulated (dashed lines) and measured (solid lines) characteristics relating to the in-phase (c) and out-of-phase (d) states.

for the out-of-phase Wilkinson power divider, i.e. 8 mm × 10 mm. The size reduction is 6 times as compared to the conventional rat-race ring on the same substrate. According to the results of EM simulation (Fig. 6 c and -d), the operational frequency band of the rat-race ring estimated at the 20 dB level of both the return loss and the isolation amounted to 45%. Hence, the operational bandwidth was broadened by the factor of 1.5 over the conventional version. Measured characteristics of the miniature rat-race ring are also plotted Fig. 6-c and -d. A good agreement between the simulated and measured characteristics of the device is observed.

IV. Conclusion

Designs of miniature LTCC in-phase and out-of-phase Wilkinson power dividers based on artificial RH and LH TL sections have been presented. An approach to design of a broadband reconfigurable 0°/180° Wilkinson-type power divider has been proposed. The results of experimental investigation of the miniature LTCC rat-race ring that is a core of the reconfigurable power divider have been presented. The results obtained show a high potential of the concept proposed and the devices designed.

Acknowledgment

References

[1] I.B. Vendik, O.G. Vendik, D.V. Kholodnyak, E.V. Serebryakova, and P.V. Kapitanova, „Digital phase shifters based on right- and left-handed transmission lines", *Proc. of European Microwave Association*, Vol. 2, No. 2, pp. 30-37, 2006.

[2] D. Kholodnyak, P. Kapitanova, S. Humbla, R. Perrone, J. Mueller, M.A. Hein, and I. Vendik (2008), „180° power dividers using metamaterial transmission lines", in *Proc. of 14-th Conf. on Microwave Techniques (COMITE-2008)*, Prague, Czech Republic, pp.169 172.

[3] M.A. Antoniades and G.V. Eleftheriades, „A broadband Wilkinson balun using microstrip metamaterial lines", *IEEE Antennas and Wireless Propagation Lett.*, Vol. 4, pp. 209–212, 2005.

[4] D. Kholodnyak, P. Kapitanova, I. Vendik, S. Humbla, R. Perrone, J. Müller, and M.A. Hein, „Novel Wilkinson-type power dividers based on metamaterial transmission lines", in *Proc. of 38th European Microwave Conference*, Amsterdam, The Netherlands, 2008, pp. 341-344.

[5] Q. Guo, Y. Ma, and J. Ju, „A novel broadband high-power combiner", in *Proc. of Asia-Pacific Microwave Conference*, Suzhou, China, 2005, Vol. 5, 4 pp.

[6]   I. Munina, P. Kapitanova, and D. Kholodnyak, "Miniaturized broad-band LTCC directional coupler using right/left-handed transmission lines", *ACTA Universitatis Ouluensis, Series C Technica*, Vol. 323, pp. 29-38, 2009.

Time-Domain Analysis of Fast Phenomena in Signal Transmission Structures

Hannes Toepfer, Thomas Ortlepp

Department of advanced Electromagnetics, Ilmenau University of Technology,
P.O. Box 10 05 65, D-98684, Ilmenau, Germany
Telephone: +49 3677 69 2629, Fax: +49 3677 69 1152,
E-mail: hannes.toepfer@tu-ilmenau.de

Abstract

As both operation speed and level of miniaturization of microelectronic systems increase, a careful design of signal-transmitting structures such as, e.g., transmission lines of via transitions, becomes more and more necessary. Especially, the effect of discontinuities may become of significant influence. Numerical timedomain approaches provide for a possibility to study the effect of given set-ups on a propagating along the structure. One of the prominent analysis methods is given by the Finite-Difference Time-Domain technique which is based on the discretisation of Maxwells equations. The contribution describes possibilities of incorporating material peculiarities into this method with special respect to the material system of superconductors. The application in selected studies of signal propagation is described and illustrated with special emphasis to fast transient cases. The application potential of this analysis approach is discussed.

I. Introduction

For many purposes in microwave engineering, the use of superconducting components can be of advantage. The development of such applications is essentially dependent on the availability of a tractable model which is suitable to be used in design and analysis software. In the design of microwave circuits, numerical methods find wide-spread application. Among them,

time-domain methods provide for insight especially into non-stationary processes such as the propagation of signals. The usual assumption of constant material parameters does not hold when the bandwidth considered is sufficiently large. For such cases, we developed a model to be used within the Finite-Difference Time-Domain (FDTD) technique. In this contribution, we restrict the consideration to the class of superconducting materials as these allow the realization of ultra-fast electronic systems. The modeling is based on Mei's description of a superconductor as a dielectric material with negative permittivity [1]. Previous works in [2, 3] are based on the difference approximation of the first London's equation. In our approach, similar as the treatment of dispersive materials in time-domain computation in [4] a recursive update formulation has been developed for the superconductor.

II. Description of superconductors for FDTD

A phenomenological description of the electrodynamics of superconductors is given by supplementing Maxwell's equations with the London equations:

$$\frac{\partial}{\partial t}\left(\mu_0\lambda^2\mathbf{J}_s\right) = \mathbf{E} \ , \tag{1}$$

$$\nabla \times (\lambda^2\mathbf{J}_s) = -\mathbf{H} \tag{2}$$

with J_s: the superconducting current density. The characteristic length λ of magnetic field penetration into the superconductors is related to microscopic quantities by $\lambda^2 = m/\mu_0 n_s e^2$ where m and e are the electron mass and charge, respectively. Within this model, for finite temperatures below the critical temperature T_c there is a coexistence of normal and super-current:

$$\mathbf{J} \quad = \quad \mathbf{J}_s + \mathbf{J}_n \tag{3}$$

carried by normal and superconducting charge carriers with densities n_n and n_s, respectively. Using (1) and (3), a relation between current density and electric field can be established as

$$\mathbf{J} = \sigma \cdot \mathbf{E} = (\sigma_1 - j\sigma_2) \cdot \mathbf{E}. \tag{4}$$

Expressions for σ_1 and σ_2 can be derived from (1) and (4) by assuming a harmonic excitation with radian frequency ω

$$\sigma_1 = \frac{n_n e^2 \tau}{m(1 + \omega^2 \tau^2)} \;, \tag{5}$$

$$\sigma_2 = \frac{n_s e^2}{\omega m} + \frac{n_n e^2 \omega^2 \tau^2}{\omega m(1 + \omega^2 \tau^2)} \;, \tag{6}$$

where τ is the momentum relaxation time. For frequencies where $\omega^2\tau^2 << 1$, (5) and (6) can be simplified essentially, resulting in:

$$\sigma_1 = \frac{n_n e^2 \tau}{m}, \quad \sigma_2 = \frac{n_s e^2}{\omega m} = \frac{1}{\omega \mu_0 \lambda^2} \;. \tag{7}$$

With typical values of $\lambda \approx 10^{-8} - 10^{-7}$ m and $\tau \approx 10^{-13} - 10^{-12}$ s, σ_2 will dominate the current transport for a large frequency range. Therefore, it is suitable to introduce a complex permittivity [1] which after separation into real and imaginary parts is given by

$$\varepsilon_r(\omega) = 1 - \frac{\omega_s^2}{\omega^2} - \frac{\omega_n^2 \tau^2}{\omega^2 \tau^2 + 1} - j\frac{\omega_n^2 \tau}{\omega(\omega^2 \tau^2 + 1)} \tag{8}$$

where

$$\omega_s^2 = \frac{e^2 n_s}{m \varepsilon_0}, \quad \omega_n^2 = \frac{e^2 n_n}{m \varepsilon_0} \tag{9}$$

are the plasma radian frequencies for the normal and superconducting charge carriers. Then the current in Ampere's law can be considered as a displacement current with the electric flux density given by

$$\mathbf{D} = \varepsilon(\omega)\mathbf{E} \;. \tag{10}$$

This expression is in compliance with the standard FDTD formulation. The complex permittivity can be decomposed into a static and a frequency-dependent component:

$$\varepsilon(\omega) = \varepsilon_0 \varepsilon_r(\omega) = \varepsilon_0 \left(1 + \chi(\omega)\right) \;. \tag{11}$$

In (11), the superconductive effects are related to the electric field and the susceptibility $\chi(\omega)$ contains the particular information about the frequency dependence.

III. Time-Domain Implementation

By means of discretization of Maxwell's curl equations in space and time the spatial and time derivatives are approximated by finite differences which provides an explicit system of equations for the field components. For including dispersive material relationships into time-domain computation several methods are known. For better memory management, the present implementation is based on the convolution approach. This required a conversion of (10) into the time domain and was done as was shown in [5] for some materials with frequency-dependent properties. After discretization in time $t \rightarrow n\Delta t$ we obtain

$$
\begin{aligned}
\mathbf{D}(t) &\approx \mathbf{D}(n\Delta t) = D^n \\
&= \varepsilon_0 \mathbf{E}(n\Delta t) + \varepsilon_0 \int_0^{n\Delta t} \chi(t')\mathbf{E}(n\Delta t - t')dt' \ .
\end{aligned}
\tag{12}
$$

Assuming that all field quantities are constant within a time step Δt, the past values of E can be extracted from the kernel of the convolution integral:

$$
D^n = \varepsilon_0 E^n + \varepsilon_0 \sum_{m=0}^{n-1} E^{n-m} \int_{(m)\Delta t}^{(m+1)\Delta t} \chi(t')dt' \ .
\tag{13}
$$

In order to maintain the same notation as in [5] we utilize the abbreviations

$$
\chi^m = \int_{m\Delta t}^{(m+1)\Delta t} \chi(t)dt \ \text{ and } \ \Delta\chi^m = \chi^m - \chi^{m+1} \ .
\tag{14}
$$

Here, m counts the past time steps from 0 to $n\Delta t$. Deriving explicitly E^n and E^{n+1} at the grid positions i, j, k and inserting them into the finite-difference expression of Ampere's law yields the update equations for every time step. For the E_x-component this is given by:

$$E_x\big|_{i,j,k}^{n+1} = \xi\left(\eta E_x\big|_{i,j,k}^{n} + \varepsilon_0 \sum_{m=0}^{n-1} E_x\big|_{i,j,k}^{n-m}\Delta\chi_{i,j,k}^{m}\right) +$$

$$+ \xi\Delta t\left(\frac{H_z\big|_{i,j+\frac{1}{2},k}^{n+\frac{1}{2}} - H_z\big|_{i,j-\frac{1}{2},k}^{n+\frac{1}{2}}}{\Delta y} - \frac{H_y\big|_{i,j,k+\frac{1}{2}}^{n+\frac{1}{2}} - H_y\big|_{i,j,k-\frac{1}{2}}^{n+\frac{1}{2}}}{\Delta z}\right) \qquad (15)$$

with $\xi=[\varepsilon_0(\varepsilon_\infty+\chi^0)+\sigma_1/2\,\Delta t]^{-1}$, $\eta=(\varepsilon_0\varepsilon_\infty-\sigma_1/2\,\Delta t)$. The information about the particular time dependence of χ is contained in $\chi^0=\chi^m|_{m=0}$ and $\Delta\chi^m$. For the loss term $\sigma_1 E$, a semi-implicit averaging of the electrical field strength is used in order to match the time steps. Equation (15) represents an expression which includes the frequency-dependent nature of the processes and is well-suited for implementation into the FDTD method. As the description is based on the two-fluid model, the contributions of the normal current and super current to χ and thus to χ^0 and $\Delta\chi^m$ can be distinguished. From (9), and (11), the partial susceptibilities caused by the normal conducting charge carriers, χ_n, and the super current carriers, χ_s, follow as

$$\chi_n(\omega) = -\frac{(\omega_n\tau)^2}{1+j\omega\tau}, \quad \chi_s(\omega) = -\frac{\omega_s^2}{\omega^2}. \qquad (16)$$

The normal conductivity is given by

$$\sigma_1 = \omega_n^2\tau\epsilon_0. \qquad (17)$$

As could be expected, the expression for χ_n is exactly a description of the metallic behaviour where scattering is not neglected [6]. For this case, the derivation of a recursive formulation has already been shown in [5] and is not repeated here. In a similar way, we obtained the expressions for the superconductive contribution. Transforming $\chi_s(\omega)$ into the time-domain leads to

$$\chi_s(t) = \frac{\omega_s^2}{2}t. \qquad (18)$$

Using (14), it is straightforward to obtain the contributions from the superconducting fraction χ^0_s and $\Delta\chi^m_s$ which are needed in (15)

$$\chi_s^0 \;=\; \frac{\omega_s^2}{4}(\Delta t)^2 \;, \quad \Delta\chi_s^m = -\frac{\omega_s^2(\Delta t)^2}{2} \;. \tag{19}$$

Note that χ_s^0 and $\Delta\chi_s^m$ do not explicitly depend on t. Combining (19) with the results of [5] for the normal electrons, for which the Drude dispersion relation is supposed to hold, we find that

$$\chi^0 \;=\; \frac{\omega_s^2}{4}(\Delta t)^2 - (\omega_n\tau)^2\left[1 - e^{-\frac{\Delta t}{\tau}}\right], \tag{20}$$

$$\Delta\chi^m \;=\; -\frac{\omega_s^2(\Delta t)^2}{2} - (\omega_n\tau)^2\left[1 - e^{-\frac{\Delta t}{\tau}}\right]^2 e^{-\frac{m\Delta t}{\tau}} \;. \tag{21}$$

As was shown in [4] storing all past field values can be avoided by introducing a recursive formulation. This is carried out by replacing the sum term in (15) by an accumulation variable

$$\Psi^n = \Psi_s^n + \Psi_n^n = \sum_{m=0}^{n-1} E^{n-m}\Delta\chi^m \tag{22}$$

where the actual form of Ψ is governed by the particular $\chi(t)$. It can be shown that

$$\Psi_s^n = \Psi_s^{n-1} + \Delta\chi_s^m E^n \;. \tag{23}$$

Making use of the expressions known for the recursion of the normal conducting contribution (Eq. (8.22) in [5]), we finally obtain as the additional update equation

$$\Psi^n = \Psi_s^{n-1} + e^{-\frac{\Delta t}{\tau}}\Psi_n^{n-1} + \Delta\chi^0 E^n \tag{24}$$

with $\Delta\chi^0$ given by (21).

IV. Example – Pulse Propagation along a Superconducting Microstrip Line

The model has been used for studies of the pulse propagation along a superconducting microstrip line using the FDTD method. In Fig. 1,
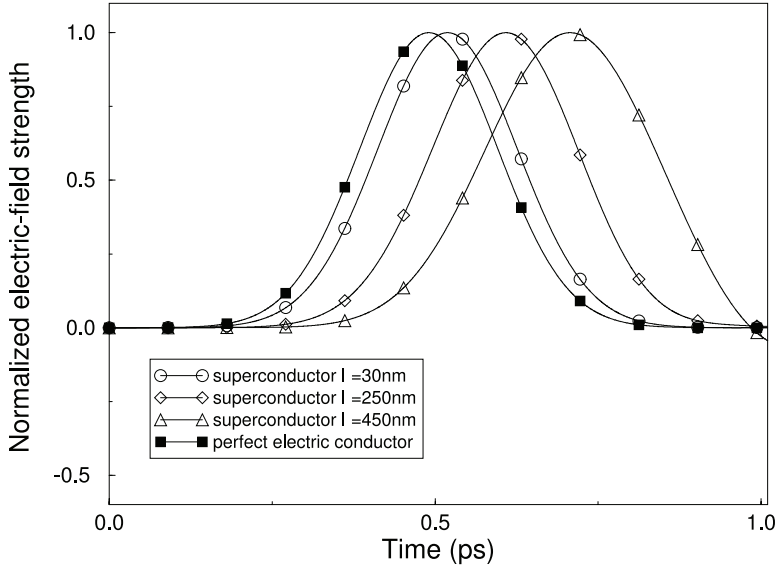
Figure 1: Waveform of a pulse propagating 5.5 µm along a superconducting microstrip line with different magnetic field penetration depths λ. For comparison, the case of a perfect electric conductor (PEC) microstrip line is shown, too.

the effect of the superconducting material properties on the propagation velocity is shown by comparing the delay of a narrow Gaussian voltage pulse propagating a distance of 5.5µm in a perfect electric (PEC) line and in a superconducting line for three different penetration depths λ. The field penetration into the interior of the material causes slower propagation which becomes evident from the calculations.

V. Conclusion

The implementation of the two-fluid model into a 3D-FDTD code provided for the possibility of broadband analyses of superconducting microwave structures. The superconducting properties are described phenomenologi-

cally in the framework of the two-fluid model using the frequency-dependent complex permittivity. The numerical results show the feasibility of this approach even for thin-film conditions. The model can be used in the analysis of transmission lines as well as of packaging interconnects made of superconductors. It has been applied in the design of a superconductive photoswitch for fast optical triggering of superconductive integrated logic circuits [7].

References

[1] Mei, K. K. and G. Liang, "Electromagnetics of Superconductors," IEEE Trans. on Microwave Theory and Techniques, Vol. 39, No. 9, 1545–1552, 1991.

[2] Xiao, S. and R. Vahldieck, "A 3D FDTD Simulation of Superconductor Coplanar Waveguides," IEEE Antennas and Propagat. Soc. Int. Symposium, Vol. 3, 1774–1777, 1994.

[3] Xiao, S. and R. Vahldieck, "An Extended 2D-FDTD Method for Hybrid Mode Analysis Lossy and Superconducting Structures," IEEE MTT-S Int. Microwave Symposium, Vol. 2, 349–352, 1995.

[4] Luebbers, R. J. and F. Hunsberger and K. S. Kunz, "A Frequency-Dependent Finite-Difference Time-Domain Formulation for Transient Propagation in Plasma," IEEE Trans. Antennas and Propagation, Vol. 39, No. 1, 29–34, 1992.

[5] Kunz, K. S. and R. J. Luebbers, Finite-Difference Time-Domain Method for Electromagnetics, CRC Press, Boca Raton, Ann Arbor, London, Tokyo, 1993.

[6] Dobbs, E. R., Basic Electromagnetism, Chapman & Hall, London, 1993.

[7] Febvre, P. and H. Toepfer and T. Ortlepp and B. Ebert and S. Badi and F. H. Uhlmann, "Superconducting Photosensitive Interfaces for Triggering RSFQ Circuits," IEEE Trans. Applied Superconductivity, Vol. 17, No. 1, 530–533, 2007.

Numerical timing analysis of a Josephson comparator in the presence of thermal noise

Sonja Engert, Thomas Ortlepp, Hannes Toepfer

Institute for Information Technology,
Ilmenau University of Technology, Germany

Abstract

A Josephson junction is the active device in superconducting electronics. A nonlinear differential equation is used to model the dynamic behaviour. A serial connection of two Josephson junctions is forming the Josephson comparator. For each external trigger event, only one of the two junctions is able to switch. An input current is applied to influence this decision process in a well-defined way. In a certain range of the input current the decision process is influenced by thermal noise, resulting in a decision uncertainty. This range is the so-called grey zone of the comparator, which limits the speed as well as the linearity of ultra-fast superconducting comparators to frequencies of about 40 GHz with a linearity of about 10 bits.

Stochastic differential equations can be used to describe the transient behaviour under the influence of thermal noise. We translate the stochastic differential equation in state space into a probability density for all possible states. The Fokker-Planck equation is a partial differential equation, which describes the transient evolution of this state probability. The numerical solution of the Fokker-Planck equation is numerically stable and provides much information for all possible states in one computation run.

We present an analysis of signal-dependent decision delay of a Josephson comparator and compare these results to Monte-Carlo-based circuit simulations. The aim of the study is to derive design guidelines of improved comparator circuits.

Keywords — **Josephson comparator, thermal noise, switching probability, switching time, grey zone, Fokker-Planck equation, jitter**

I. Introduction

Superconductors provide very special electrical properties. When their temperature falls below a critical temperature T_C, the electrical resistance goes to zero. A small superconducting loop provides the unique feature of flux quantization [1]. If the loop is interrupted by a weak link, the movement of magnetic flux quanta can be controlled by electrical currents.

A so-called Josephson junction is an active device in superconducting electronics. It is built by two weakly coupled superconductors separated by a nanometer-thin insulating barrier. The properties of both superconductors are described by quantum mechanical wave functions. The phase difference x across the Josephson junction is defined by the difference in the quantum mechanical phase of the two superconductors (short: phase of a junction). If a small current flows through a Josephson junction it remains superconducting. When the current exceeds the critical current I_C, the junction switches to voltage state. In this moment a short voltage pulse occurs across the Josephson junction. In Rapid Single Flux Quantum (RSFQ), the most important superconducting logic family [2], each junctions has a parallel damping resistor. This so called shunt resistor is damping the dynamic oscillations during the voltage mode. If the junction is connected to a small superconducting loop, we name a switching event which causes a phase change of 2π.

The magnetic flux in a ring is always an integer multiple of the magnetic flux quantum $\Phi_0 \approx 2.07 \cdot 10^{-15} Vs$ [1]. In order to transmit flux quantums, a Josephson transmission line (JTL) can be used. It consists of small rings interrupted by two Josephson junctions. This screening current related to one flux quantum is much larger than the critical current. Therefore, the loop is not able to store a flux quantum. One loop of a JTL is shown in Fig.1.

When the sum of the input current and the bias current of junction J1 exceeds its critical current, it is forced to switch. Thus a flux quantum is moved to the central loop and a circulating current arises in the inductor L_1. The sum of the circulating current and the bias current I_b exceeds the critical current of J2 and the flux quantum will be transmitted to the following loop by switching J2.
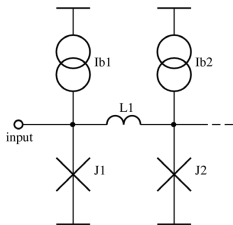
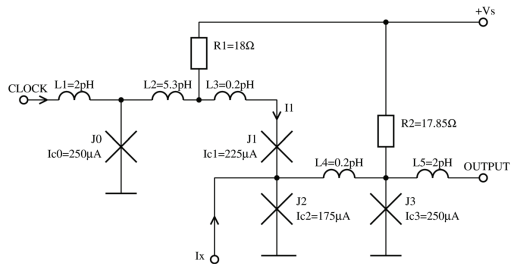**Fig. 1: Circuit diagram of one loop of a JTL.**

Fig. 2: Circuit diagram of a Josephson compara-tor including trigger and readout circuitry. For simplicity no parasitic elements are displayed.

A Josephson comparator consists of two Josephson junctions (J1, J2) connected in series as shown in Fig.2. It is used as a current depended discission element. (The results that are presented in this work do not correspond to the comparator as specified in Fig.2 and respectively Fig.4. They result from a testing circuit and are qualitative comparable.)

Each clock pulse triggers a switching event of the driver junction J0 which results in a phase change of 2π. The phase jump of x_0 results in a current
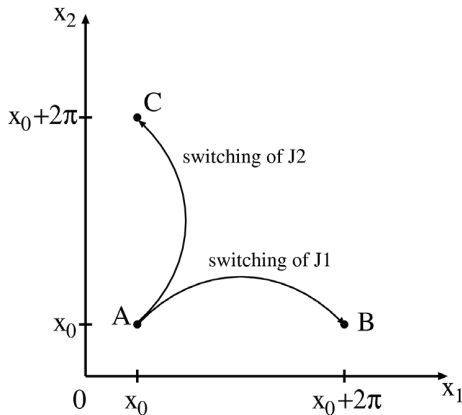

Fig. 3: Phases of the Josephson comparator before (A) and after (B or C) one of the junctions J1/J2 has switched.

pulse $I_1(t)$, which forces one of the junctions of the comparator to switch. The input current I_x between the junctions J1 and J2 influences this decision process and decides which junction will switch.

The stable states of a comparator in state space are illustrated in Fig.3. Before switching, the comparator is labelled as "A". Both phases have an initial phase value of about $x_0/2$. The comparator state changes to state "B" or "C" depending on the input signal.

Josephson comparators are a key element of superconducting Analogue-to-Digital converters (A/D converters). They outperform conventional semiconductor A/D converters in terms of speed and accuracy [3]. Nevertheless, the performance of such a comparator is limited by its switching time and its switching uncertainty, which is quantified by the grey zone. The switching uncertainty is caused by thermal noise. In order to compare different Josephson comparators, the grey zone and the switching time are numerically calculated. The results are the base to study the specific influence of all design parameters.

II. Grey zone and switching time study

Within a certain range of the input current thermal noise influences the decision process. Therefore it is not sure which one of the two junctions will switch. This range is the so-called grey zone of the comparator.

To enable a faster numerical computation of the differential equations, we introduce some simplifications, as shown in Fig.4.

We combine the junctions J2 and J3 to J2* and we simplify the clock generator and the junction J_0 to a phase source $x_0(t)$ that is described by Eq.(1):
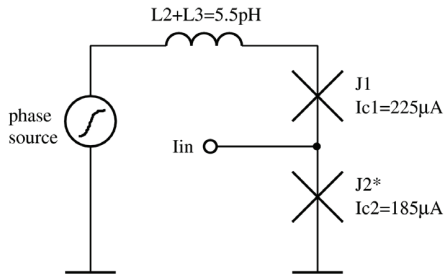

Fig. 4: Simplified circuit diagram of a Josephson comparator.

$$x_0(t) = x_{01} + 2\arctan\left(\frac{t - t_0}{a}\right) + \pi, \tag{1}$$

where x_{01} is the initial value of the phase source, t_0 is the switching time of the pulse and a is a factor that influences the pulse width which relates to the rise time of Eq.(1). This leads to new parameter values, which can also be found in Fig.4. The behaviour of the Josephson comparator under the influence of thermal noise can be described by the following stochastic differential equations (Eq. (2)):

$$\dot{x}_1 = \frac{R_1}{L}(x_0(t) - x_1 - x_2) - \frac{2\pi R_1}{\Phi_0} I_{C_1}\sin x_1 + I_{n1}(t),$$
$$\dot{x}_2 = \frac{R_2}{L}(x_0(t) - x_1 - x_2) - \frac{2\pi R_2}{\Phi_0}\left(I_x - I_{C_2}\sin x_2\right) + I_{n2}(t). \tag{2}$$

The parameters for these equations are specified as follows. The phases of the junctions are x_1 and x_2, R_1 and R_2 are the shunt resistors damping the junction dynamics, $L = L_2 + L_3$ is the loop inductance of the comparator, I_{C1}, I_{C2} are the critical currents of the Josephson junctions, I_x is the separate input current of the comparator and $I_{n1}(t)$, $I_{n2}(t)$ are the mean-free white noise currents. The standard deviations of the noise currents are σ_{n1} and σ_{n2}. Because the noise currents are indeterminate, Eq.(2) can not be solved definitely. One way out is to translate the system of stochastic differential equations into a partial differential equation, the so-called Fokker-Planck equation, which describes the transient evolution of the probability of all possible states [4]. The Fokker-Planck equation describing the simplified comparator in Fig.4 is given by Eq. (3).

$$\frac{\partial W(x_1, x_2, t)}{\partial t} = W\left(\frac{R_1}{L} + \frac{2\pi R_1}{\Phi_0} I_{C_1}\cos x_1\right) + W\left(\frac{R_2}{L} + \frac{2\pi R_2}{\Phi_0} I_{C_2}\cos x_2\right)$$
$$+ \left(\frac{2\pi R_1}{\Phi_0} I_{C_1}\sin x_1 - \frac{R_1}{L}(x_0(t) - x_1 - x_2)\right)\frac{\partial W}{\partial x_1}$$
$$+ \left(\frac{2\pi R_2}{\Phi_0}\left(I_x - I_{C_2}\sin x_2\right) - \frac{R_2}{L}(x_0(t) - x_1 - x_2)\right)\frac{\partial W}{\partial x_2}$$
$$+ \frac{1}{2}\sigma_1\frac{\partial^2 W}{\partial x_1^2} + \frac{1}{2}\sigma_2\frac{\partial^2 W}{\partial x_2^2}. \tag{3}$$
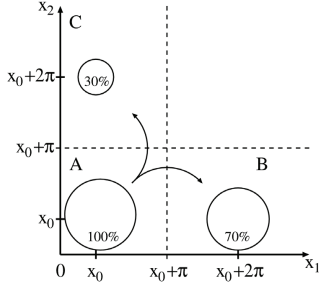
Fig. 5: Phases of the Josephson comparator before (A) and after (B or C) one of the junctions J1/J2 has switched; here x_1 has a higher switching probability.
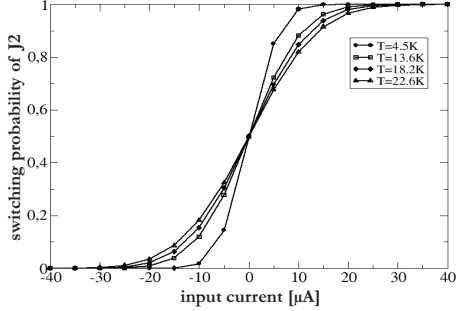
Fig. 6: Switching probability of J2 regarding different temperatures.

The function $W(x_1,x_2,t)$ is the time dependent probability distribution for all possible states (x_1,x_2). The parameters σ_{x1}, σ_{x2} are the diffusion constants. They result from the variances σ_{n1}, σ_{n2}.

The Fokker-Planck equation can be solved numerically. Its solution represents the probability for all possible states. So the areas B$=\{x_1 > x_0 + \pi$, $x_2 < x_0 + \pi\}$ and C$=\{x_1 < x_0 + \pi, x_2 > x_0 + \pi\}$ can be analysed. In area A$=\{x_1 < x_0 + \pi, x_2 < x_0 + \pi\}$ there is the initial state. The decision process depends on the input current I_x. This behaviour is demonstrated in Fig. 5. An example is shown in Fig.6. In this case the switching probability of junction J1 is 70% and the probability of junction J2 is 30%. The transition between state „A" and „B" respectively „C" is continuous.

The switching probability for one junction (J2) in cases of different temperatures is demonstrated in Fig.6. One can recognise, that the curves for lower temperatures have a steeper rise. This means that the grey zone grows when the temperature is growing. The dependency can be fitted by the root function Eq.(4) (ΔI_x =grey zone, T=temperature):

$$\frac{\Delta I_x}{\mu A} \approx \sqrt{35.1\frac{T}{K}+1.7} - 0.7. \tag{4}$$

This corresponds to the declaration in [5]. It is generally known that the function of switching probability can be approximated by the error function [6]. In Eq.(5) this is demonstrated for the switching of J2:

$$P(C) = 0.5 + 0.5\mathrm{erf}\left(\sqrt{\pi}\,\frac{I_x - \mu_x}{\Delta I_x}\right), \tag{5}$$

the threshold current is μ_x. With this equation the grey zone ΔI_x can be easily computed. It is approximately the current range where the switching probability is between 0.1 and 0.9. For every input current always both states are possible. Therefore the comparator perhaps needs very long for its decision. We define the switching time t_s of a comparator as the moment when 50% of the probability for the new state is in the area „B" or „C", as described in Eq.6.

$$\iint W(x_1, x_2, t_S)\,dx_1 dx_2 = \frac{1}{2}\lim_{t \to \infty}\iint W(x_1, x_2, t)\,dx_1 dx_2 \tag{6}$$

$$\sigma_{xi} = \int_{x_0}^{x_0 + 2\pi}(x_i - \mu_i)^2 W(x_1, x_2, t_S)\,dx_i, i = 1,2. \tag{7}$$

Fig.7 shows the switching time of the junctions subject to the input current. Fig.8 shows the standard deviation σ_{x1}, σ_{x2} of the probability distribution $W(x_1, x_2, t)$ at the switching time t_s. It was calculated by Eq.7.
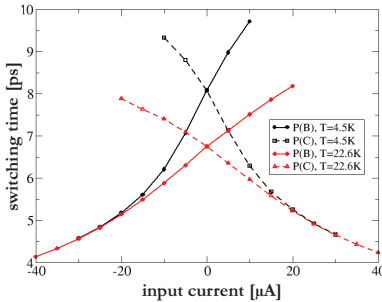

Fig. 7: Switching time of J2 regarding different temperatures dependend on the input current.
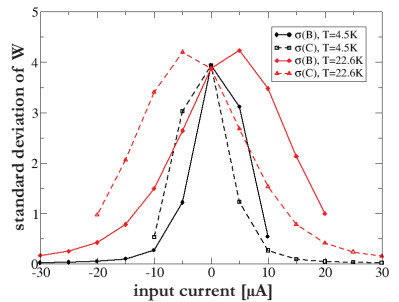
Fig. 8: Standard deviation at the switching time t_S regarding different temperatures versus the input current.
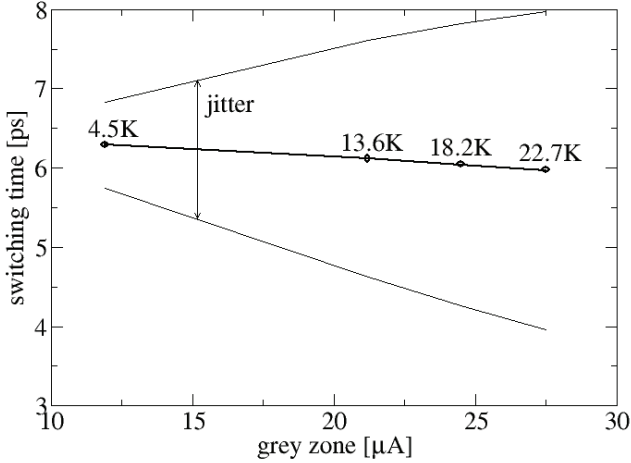
Fig. 9: Dependency of switching time and grey zone, including the uncertainty in switching time (jitter).

The mean values of W are μ_1 and μ_2. The deviation reaches a maximum in close vicinity of the threshold value, when both states („B" and „C") have the same switching probability. The maximum deviation seams not to vary with temperatures. For values far below or above the threshold, the deviation of the probability density is decreasing again.

There is any correlation between the standard deviation and the uncertainty in switching time (jitter). So Fig.8 gives a qualitative description of the jitter. In Fig.9 grey zone and switching time were calculated for different temperatures. One can recognise, that there is any relationship between these attributes. When the grey zone shall be reduced, the switching time grows.

III. Conclusion

In this paper we described a method of a one-step calculation of the grey zone and the switching time of a Josephson comparator. This method also gives information about the phase values and variances (jitter) at any time during the simulation. This is a reasonable alternative to the Monte-Carlo-based methods, which need a large amount of calculation steps.

Our intention is to reduce the simplifications and expand the method for calculating the grey zone including all circuit parameters and parasitics. Furthermore the relationship between the grey zone and the switching time is not specified. Knowledge about it could enable to design Josephson comparators targeted on each application

Acknowledgment

References

[1]   R. Doll, M. Näbauer, "Experimenteller Nachweis der Quantisierung eingefrorener Magnetflüsse im supraleitenden Hohlzylinder" Zeitschrift für Physik, pp. 169, 526-563, Jul. 1962

[2]   K. K. Likharev, V. K. Semenov, "RSFQ logic/memory family: a new Josephson-junction technology for sub-terahertz-clock-frequency digital systems " IEEE Trans. Appl. Supercond., vol. 1, no.1, pp. 3-28, Mar. 1991

[3]   O. A. Mukhanov, D. Gupta, A. M. Kadin and V. K. Semenov, "Superconductor Analog-to-Digital Converters" Proc. of the IEEE, vol. 92, no. 10, pp. 1564–1584, Oct. 2004

[4]   Q. P. Herr, D. L. Miller and J. X. Przybysz, "Josephson comparator switching time" Supercond. Sci. Technol., vol. 19, pp. 387–389, 2006

[5]   T. V. Filippov, V. K. Kornev, "Sensitivity of the Balanced Josephson-Junction Comparator" IEEE Trans. on Magnitics, vol. 27, no. 2, pp. 2452-2455, Mar. 1991

[6]   B. Ebert, O. Mielke, J. Kunert, R. Stolz and T. Ortlepp, "Experimentally verified design guidelines for minimizing the gray zone width of Josephson comparators" Supercond. Sci. Technol., vol. 23, 055005, 2010

Superconducting electronics with complementary circuit elements based on novel material combinations

O. Wetzstein[#1], Th. Ortlepp[#2], J. Kunert[#1], H. Toepfer[#2]

[#1]*Department of Quantum Detection / Institute of Photonic Technology e.V.,*
P.O. Box 100239, D-0770, Jena, Germany.
[#2]*Department of Advanced Electromagnetics / Ilmenau University of Technology,*
P.O. Box 100565, D-98684 Ilmenau, Germany

Abstract

Superconducting Rapid Single Flux Quantum (RSFQ) electronics is based on fundamental characteristics of superconducting material like lossless direct current transfer and flux quantization in superconducting loops. This results in an intrinsically digital and extremely fast electronics (above 100 GHz) in combination with extremely low energy consumption ($2 \cdot 10^{-19}$ J per switching event). The electronics is based on the controlled exchange of single flux quanta between adjoining loops. The Josephson junction is the active component acting like a gate between the loops controlling the flux transfer.

Novel fabrication technologies are providing new material combinations, which allow the creation of a new circuit element for RSFQ electronics. This element is the complementary element to the Josephson junction. We present RSFQ circuits utilizing the d-wave symmetry of high temperature superconductors and suggest a method to apply a Josephson junction containing a ferromagnetic barrier. Both novel material combinations are providing a complementary Josephson junction.

We analyze the impact of this new circuit element on the quality of RSFQ circuits. We compare by simulation studies and experiments the operation range of conventional RSFQ electronics with circuits containing complementary Josephson junctions. Additionally, we demonstrate an improved robustness against parameter variations caused by the fabrication process.

I. Introduction

The rapid single flux quantum electronics is a pulse driven naturally ultra fast integrated circuit family where the information is represented by the magnetic flux quantum with the Planck's constant and the elementary charge [1]. It consists of superconducting loops interrupted by a well defined barrier called Josephson junction [2]. The Josephson junction is the active element acting like a gate controlling the exchange of flux quanta between adjoining loops. While this transfer the junction switches into a voltage state for the very short time period of some pico seconds. RSFQ circuits are typically composed of three components namely: inductors, current sources and Josephson junctions. Based on them, three basic structures for transfer, storage and decision can be constructed [3].

The energy consumption of a single switching event of a Josephson junction is extremely low, in the region of $2 \cdot 10^{-19}$ J. In contrast to normal conductors, all charge carriers in a superconductor can be described by one and the same quantum mechanical wave-function. The wave-function is defined by amplitude and phase. The quantum mechanical phase difference φ of the wave-function across an element is used as new state variable characterizing the behaviour similar to the voltage in normal conductor circuits. The elements of RSFQ are current controlled, thus a circuit element is characterized by its current-phase relation.

Since the pulse driven nature of RSFQ electronics the capability of temporary data storage is important for every logic device. A superconducting loop which is able to store a flux quantum is a naturally tristable system [4], thus a bistable characteristic has to be artificially created. Usually a bias current source is used to restrict the number of stable states. Often this current has to be injected between the junction pair of a comparator. This injection spot is very sensitive to any parameter variation, so the biasing perturbs the decision process of the comparator. This is a drawback for the resulting device, which restricts the area of operation.

Using Phase Shifting Elements (PSE) to establish a bistable data storage as

proposed in [5] is an expedient approach to provide a bistable circuit characteristic without any negative influence on comparator configurations. A PSE is characterized by an additional current independent phase offset in their current-phase relation called phase shift. PSE can be artificially constructed using RSFQ standard components with the drawback of increased circuit complexity. A straightforward solution is the application of a new circuit element called π-junction. It is the complementary element [6] to the Josephson junction. The current-phase relation of both elements differs only by a π-phase shift. The π-junction can be created by novel material combinations and delivers PSE without any extra wiring or additional circuit parts. Similar to classical Complementary Metal Oxide Semiconductor (CMOS) technology the complementary element enables an unsurpassed symmetry leading to relaxed condition for the circuit design and an improved robustness against parameter variation caused by the fabrication process [4].

II. π-Phaseshifter

The π-phaseshifter is an artificially constructed PSE. It is composed of a single flux quantum stored in a superconducting loop [7]. A sketch of this device, together with the schematic, is illustrated in Fig. 1. The π-phaseshifter is connected at opposite sides. So, the overall loop inductance $L_{loop} = 2L$ is segmented into two equal parts. Thus, the effective inductance between the terminals is half of the inductance of each branch L/2. If the inductance L1 of the terminals can be neglected, the current-phase relation of this device is given by:

$$\varphi(I) = n\pi + \frac{\pi L I}{\Phi_0}. \tag{1}$$

Thereby n is the number of flux quanta stored in the loop [8]. If one single flux quantum is stored in the loop (n = 1), the ground state with I = 0 is characterized by a phase shift of π. Connected with the stored flux quantum is a current I_{loop} circulating in the loop. The device behaves like a π-junction in small signal range [4].

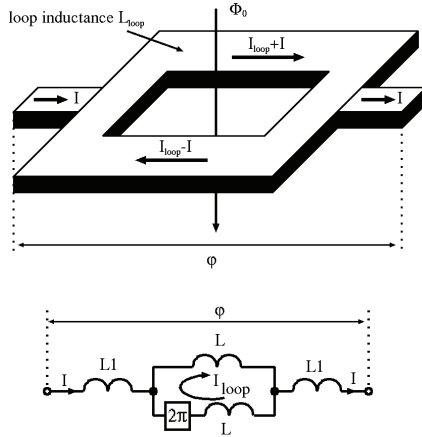The π-phaseshifter can be easily implemented into standard Niobium tech-

Fig. 1 The sketch and the schematic diagram of a π-phaseshifter, which consists of a superconducting loop and a stored single flux quantum.

nology [9] without any modifications of the fabrication process, which is of great advantage [10]. To investigate the influence of a phase shifting element on the circuit characteristic we investigated a Toggle Flip-Flop (TFF) illustrated in Fig.2 [1]. The core of the TFF is composed of two comparators (J4, J2) and (J5, J3) coupled by the inductance L. If a flux quantum enters the TFF cell input and pass trough J1, the junctions of the core will switch in pairs J2 and J5 or J3 and J4 depending on the direction of the cur-
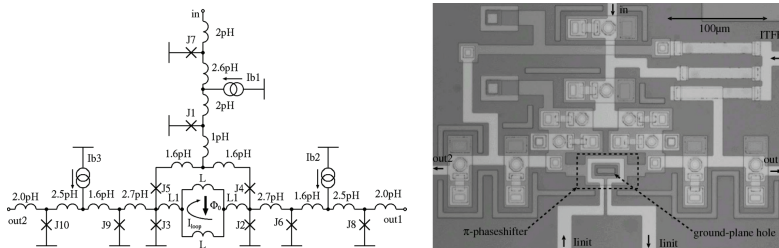

Fig. 2 (left) Schematic of a TFF with implemented π-phaseshifter. (right) A microphotograph of the TFF which was fabricated by FLUXONICS Foundry [9].
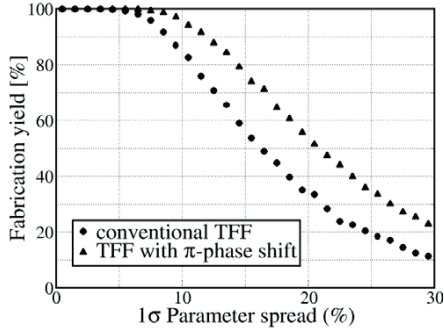
30

Fig. 3 Simulation of fabrication yield for our best conventional TFF in comparison to a realization containing a π-phaseshifter. All circuit parameter are normal distributed around their design values with the given standard deviation σ.

rent I_{store} flowing in the ring of J2-PSE-J3. This circulating current represents the internal logical state of the flip-flop. For each input pulse the state toggles between "0" and "1" which directly corresponds to the number of flux quanta stored in the ring.

A Monte Carlo variation of all circuit parameters was performed to analyze the stability of the flip-flop against variations caused by the fabrication process. Therefore several thousand parameter-sets which had normal distributed random values with a certain standard deviation σ for all adjustable parameters (critical currents, inductances and bias currents) were assigned to the device. Its correct operation was checked by automatic circuit simulation runs. The results are illustrated in Fig. 3 and show a significantly improved robustness of the circuit caused by the implemented phase shifting element.

The minor drawback is the necessary initialization of the π-phaseshifter. During the transition of the chip from normal to superconducting state, a single flux quantum needs to be frozen in each π-phaseshifter, the process is called initialization. There for a magnetic flux created by the current I_{init} is inductively coupled to the π-phaseshifter during the cooling-down of the chip (Fig. 2). We experimentally demonstrated the reliable initialization [11]. However, the initialization procedure caused additional wiring on the chip
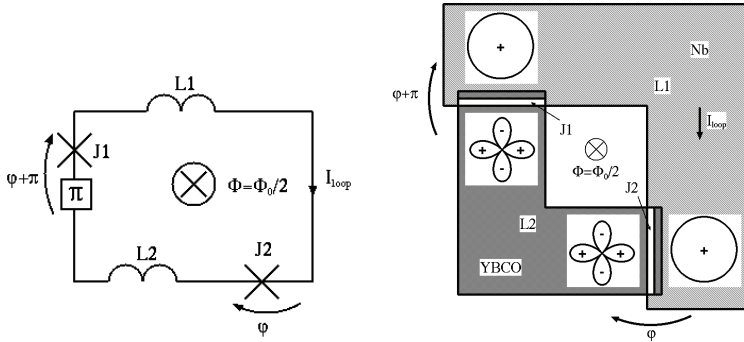
Fig. 4 The schematic and the layout of a superconducting loop comprising YBCO and Nb material. A spontaneous current arises by connecting the YBCO area with Nb from perpendicular directions.

which can be avoided by using a phase shifting element based on special material characteristics.

III. Combining HTS and LTS Material

The combination of high temperature superconducting (HTS) material and low temperature superconducting (LTS) material allows the creation of π-rings. They consist of inductors (L1 and L2) two Josephson junctions and a π-phase shift as illustrated in Fig. 4. The phase shift results from the d-wave symmetry of the HTS material [12]. YBCO is the utilized HTS
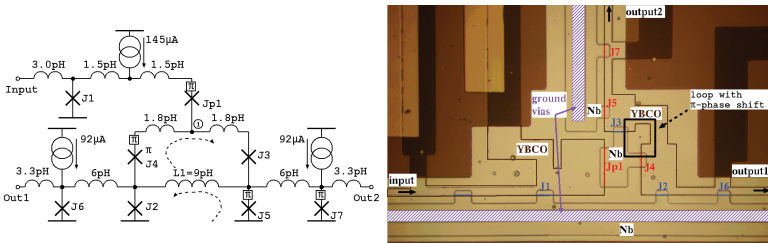

Fig. 5 (left) Schematic of the TFF utilizing π-rings. (right) Microphotograph of a TFF with π-rings fabricated at the University of Twente. One of the loops containing a π-phase shift is marked.

material and Niobium (Nb) is the LTS material. A π-ring is formed by connecting one YBCO area with Nb from perpendicular directions like illustrated in Fig. 4. This phase offset occurs at one of the junctions, thus in the equivalent circuit of one Josephson junctions can be merged with the phase shift to a π-junction. The source of the phase shift has no influence on effect to the circuit behaviour. Thus, utilizing a π-junction comes up with the same positive effect on RSFQ logic devices like the π-phaseshifter do, but without additional efforts for initialization the π-phaseshifter needs. The first successful realization of a digital circuit containing active junctions with intrinsic phase shifts exemplifies a TFF whose core is composed of π-rings (Fig.5) [13]. This device behaves like the mentioned standard TFF, while the equivalent network displayed in Fig.5 differs in some details. There are several restrictions during the layout process as consequence of the d-wave symmetry of YBCO. The relative orientation of the junctions within a loop determinates π-rings and conventional rings. Thus, the orientation of a junction becomes restricted. For example, the junction J7 of the JTL connected to an output of the TFF requires the same orientation as the output junction J5 (Fig.5).

IV. SFS-SIS hybrid technology

The barrier material of SIS-Josephson junction is an insulator. Such kind of Josephson junctions are used in standard Nb-technology [9]. The barrier of SFS-junctions consists of ferromagnetic material. Depending on the barrier thickness SFS-junctions are a conventional Josephson or a π-junction [14]. For $Ni_{0.6}Cu_{0.4}$ alloy the barrier thickness between 6 nm < d < 9 nm creates a π-junction at T=4.2 K [14]. A SFS-technology provides π-junctions as lumped elements independent of any constructed loops or environmental circuits and it is therefore a very universal solution. One possible advantage of a SFS-technology is a reduced number of restrictions resulting directly in a relaxed design process.

At the time, the electrical properties of available SFS-junctions are a serious problem, if one going to use them as active switching element. The characteristic voltage I_CR_N is defining the maximum available clock frequency of RSFQ circuits by [16]. In RSFQ circuits the critical current of a junction
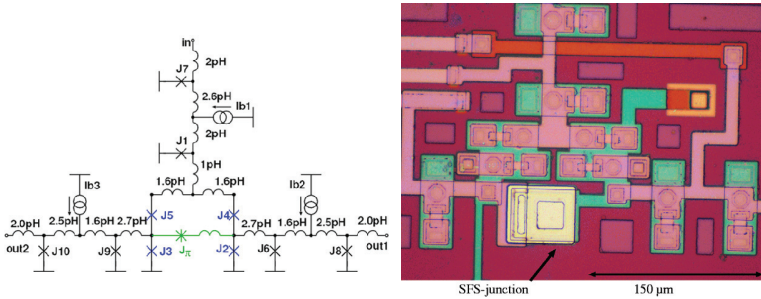
Fig. 6 (left) Schematic of a TFF with a passive π-junction. (right) Microphotograph of the TFF fabricated using SFS-SIS hybrid technology. The SFS-technology of FZ Jülich [15] in combination with standard Nb-technology of FLUXONICS Foundry [9] was used.

should be I_C>100 μA to avoid a crucial influence of thermal noise. The current available SFS-junction with I_C>100 μA have an intrinsic resistance R_N≈1 mΩ resulting in f_{max}≈10 MHz. Consequently, RSFQ circuits with active switching π-junctions are not appropriate for high clock frequencies. A possible solution was mentioned in [5]. Thereby only the phase shift of the π-junctions was utilized as circuit element. Like illustrated in Fig. 6 the SFS-junction can be used in passive mode. That means all active circuits parts are produced as Josephson junction in a standard technology with electrical properties which are appropriate for clock frequencies up to 40 GHz. The SFS-junction only creates the π-phase shift in the storing loop and do not switch. In this case the critical current of the junction is the only im-
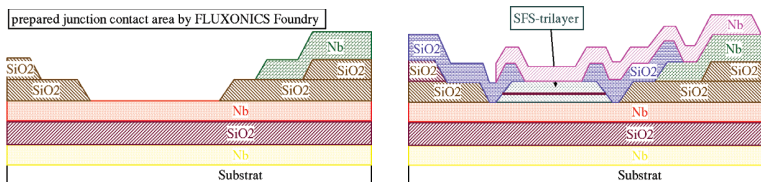

Fig. 7 Cross-section of the SFS-SIS hybrid technology. (left) The active parts of the circuit are fabricated by FLUXONICS Foundry using their standard Nb-technology. (right) A planar contact area is prepared in which the SFS junction can be nested using the SFS-technology of FZ Jülich.

34

portant parameter and must be $I_C > 100$ µA. Such junction can be fabricated using the SFS-technology of FZ Jülich. Thus, we used the standard Nb-technology of FLUXONICS Foundry [9] creating the active parts of the circuit and the SFS-technology (FZ Jülich) to fabricate the π-junction [15]. The method to implement the SFS-junction is illustrated in Fig. 7.

In the standard technology a 25 µm * 25 µm contact area for the SFS-junction is prepared. It is important that this area is planar. Than a 20 µm * 20 µm SFS trilayer is fabricated. So one electrode becomes automatically connected to the RSFQ circuit, the other one becomes connected by a new Nb-layer. A similar circuit based on related technologies was successfully demonstrated in [17].

V. Conclusion

We demonstrated improved circuit robustness against parameter variations caused by the fabrication process by implementing phase shifting elements. We mentioned three different solutions for phase shifting elements, each one with an associated fabrication technology. The π-phaseshifter is available in standard Nb-technology, which is a big advantage concerning the technology reliability. Furthermore, we mentioned two novel material combinations; the HTS-LTS-technology and the SFS-SIS hybrid technology. Both provide a phase shifting element based in the material characteristic. Thus, an initialization procedure as the π-phaseshifter needs is not necessary. That reduces the circuit complexity because no initialization network is required and improves the circuit reliability.

For the circuit design purposes the SFS-SIS hybrid technology is the best solution, because it is the only technology which provides lumped element π-junctions. This results in relaxed design restrictions.

Acknowledgment

References

[1]   K. Likharev and V. Semenov, "RSFQ logic/memory family: A new Josephson junction technology for sub-terahertz-clockfrequency digital systems," IEEE Trans. Appl. Superconductivity, vol. 1, no. 1, pp. 3–27, 1991.

[2]   B. Josephson, "Possible new effects in superconductive tunnelling," Phy. Let, vol. 1, no. 7, pp. 251–253, 1962.

[3]   D. Brock, E. Track, and J. Rowell, "Superconductor ICs: the 100-GHz second generation," IEEE Spectrum, vol. 37, no. 12, pp. 40–46, 2000.

[4]   T. Ortlepp, Ariando, O. Mielke, C.-J.-M. Verwijs, K.-F.-K. Foo, A. Andreski, H. Rogalla, F.-H. Uhlmann, and H. Hilgenkamp, "RSFQ circuitry using intrinsic π-phase shifts," IEEE Trans. Appl. Superconductivity, vol. 17, no. 2, pp. 659–663, 2007.

[5]   A. Ustinov and V. Kaplunenko, "Rapid single-flux quantum logic using π-shifters," Journal of Applied Physics, vol. 94, no. 8, pp. 5405–5407, 2003.

[6]   E. Terzioglu, D. Gupta, and M. Beasley, "Complementary Josephson junction circuits," IEEE Trans. Appl. Superconductivity, vol. 7, no. 2, pp. 3642–3645, 1997.

[7]   J. Majer, J. Butcher, and J. Mooij, "Simple phase bias for superconducting circuits," Applied Physics Letters, vol. 80, no. 19, pp. 3638–3640, 2002.

[8]   O. Mielke, T. Ortlepp, B. Dimov, and F. Uhlmann, "Phase engineering techniques in superconducting quantum electronics," J. Phys.: Conf. Ser., vol. 97, no. 012196, p. 9, 2008.

[9]   FLUXONICS, "FLUXONICS-foundry," http://www.fluxonics-foundry.de/, 2009.

[10] D. Balashov, B. Dimov, M. Khabipov, T. Ortlepp, D. Hagedorn, A. Z. F.-I. Buchholz, F. Uhlmann, and J. Niemeyer, "Passive phase shifter for superconducting Josephson circuits," IEEE Trans. Appl. Superconductivity, vol. 17, no. 2, pp. 142–145, 2007.

[11] O. Mielke, T. Ortlepp, J. Kunert, H.-G. Meyer and H. Toepfer, "Controlled initialization of superconducting π-phaseshifter and possible applications," Supercond. Sci. Technol., vol. 23, No. 055003, (7 pp), 2010.

[12] D. Wollmann, D. V. Harlingen, W. Lee, D. Ginsberg, and A. Leggett, "Experimental determination of the superconducting pairing state in YBCO from the phase coherence of YBCO-Pb dc-SQUIDs," Physical Review Letters, vol. 71, no. 13, pp. 2134–2137, 1993.

[13] T. Ortlepp, Ariando, O. Mielke, C. Verwijs, K. Foo, H. Rogalla, F. Uhlmann, and H. Hilgenkamp, "Flip-Flopping fractional flux quanta," Science, vol. 312, no. 5779, pp. 1495–1497, 2006.

[14] V. Ryazanov, V. Oboznov, A. Rusanov, A. Veretennikov, A. Golubov, and J. Aarts, "Coupling of two superconductors through a ferromagnet: Evidence for a π-junction," Physical Review Letters, vol. 86, no. 11, pp. 2427–2430, 2001.

[15] M. Weides, M. Kemmler, E. Goldobin, D. Koelle, R. Kleiner, H. Kohlstedt, and A. Buzdin, "High quality 0 and π-Josephson tunnel junctions," Applied Physics Letters, vol. 89, p. 122511, 2006.

[16] V. K. Kaplunenko, "Fluxon interaction in an overdamped Josephson transmission line," Applied Physics Letters, vol. 66, p. 3365, 1995.

[17] M.I. Khabipov, D.V. Balashov, F. Maibaum, A.B. Zorin, V.A. Oboznov, V.V. Bolgnov, A.N. Rossolenko and V.V. Ryazanov, "A single flux quantum circuit with a ferromagnetic-based Josephson π-junction," Supercond. Sci. Technol., vol. 23, No. 045032, (6 pp), 2010.

Slotted-Waveguide Antennas for Mobile Satellite Communications at 20 GHz

E. Schäfer[#1], J. Steinwandt[#2], H. Bayer[#3], A. Krauss[#3], R. Stephan[#3], and M. A. Hein[#3]

[#1] *Electronic Circuits and Systems Laboratory,*
[#2] *Communications Research Laboratory,*
[#3] *RF and Microwave Research Laboratory,*
Ilmenau University of Technology, Germany

Abstract

In this paper, two different concepts for slotted waveguide antennas, namely crossed and inclined slots, are evaluated with respect to applications as user terminals for mobile satellite communications at Ka-band frequencies. The assembly of multiple individual slot pairs at the broad side of a waveguide behaves like a linear array of slot pairs. The geometrical arrangement of these pairs and the coupling between them limit the degrees of freedom to shape the radiation pattern and cause perturbing grating lobes. These drawbacks are studied by simulations and analytical considerations. For experimental verification, a special waveguide structure including a printed circuit board (PCB) for one broadside was designed and manufactured. This PCB includes all slot pairs, formed by a standard etching process. A model of this device was implemented in a full-wave field simulator, in order to facilitate further optimisation. Finally, suitability for satellite applications is evaluated based on the results obtained so far.

Keywords — **slotted-waveguide antenna, circularly polarised, crossed slots, inclined slots**

I. Introduction

For mobile satellite communications, novel antenna concepts suitable for low-profile devices are highly desirable. Circularly polarised radiation is of

special interest here. At Ka-band frequencies, i.e., at 30 GHz for the uplink (from terminal to satellite) and around 20 GHz for the downlink (from satellite to terminal), the antenna feeds usually consist of waveguides. This motivates the idea to use the waveguides also as radiating elements [1]. These so called slotted-waveguide antennas are very popular for high-frequency applications, like synthetic-aperture radar (SAR) [2]. They feature high radiation efficiency and antenna gain, high polarisation purity, and their fabrication is simple and inexpensive. While slotted-waveguide antennas for linearly polarised radiation are widely represented in literature, constructing circularly polarised slot antennas is a more sophisticated task, as they require more design constraints to be met. Over the last decades, many designs have been suggested and analysed. In 1957, A. J. Simmons used two crossed slots (a so-called X-slot) to radiate circularly polarised waves by placing them at a proper position along the broadside face of a rectangular waveguide [3]. Later on, A. F. Seaton and G. A. Carnegis extended this design to build an antenna array composed of crossed-slot radiators for the Surveyor spacecraft [4]. In 2004, G. Montisci et al. suggested a configuration of two non-crossing, very closely spaced, inclined slots for circular polarisation with a very low axial ratio [5]. Based on these contributions, we examine and compare their suitability for mobile satellite communications at Ka-band frequencies, with the focus on the downlink frequency at 20 GHz. The design of both types of antennas, crossed slots and non-crossing slots, is described in Section II. To obtain a simple experimental verification, a special waveguide structure including a printed circuit board (PCB) for one broadside was developed, as described in Section III. Section IV provides an analysis of the simulation and measurement results.

II. Designs of Circularly Polarised Slotted-Waveguide Antennas

A. Crossed-slots antenna
According to Babinet's principle, a slot antenna is the dual counterpart of a dipole [6]. In analogy with a dipole excited by a voltage source, slot antennas are stimulated by surface currents.

The transverse and longitudinal magnetic fields of the fundamental H_{10} mode excited in a rectangular waveguide of width a are given by

$$H_x = H_0 \sqrt{1 - \left(\frac{\lambda_0}{2a}\right)} \sin\left(\frac{\pi x}{a}\right), \tag{1}$$

$$H_y = -jH_0 \left(\frac{\lambda_0}{2a}\right) \cos\left(\frac{\pi x}{a}\right). \tag{2}$$

From these equations and the angular relation between the magnetic fields and the surface current,

$$\mathbf{J} = \mathbf{n} \times \mathbf{H}, \tag{3}$$

it follows that at all points on the broad face where the condition $|H_x| = |H_y|$ is met, i.e. where

$$x_{1,2} = \frac{a}{\pi} \operatorname{arccot}\left(\pm \sqrt{\left(\frac{2a}{\lambda_0}\right)^2 - 1} \right), \tag{4}$$

the surface current density is circularly polarised in the *x-y* plane. In these equations, $\mathbf{J}$ is the surface current vector, $\mathbf{H}$ describes the magnetic field strength, and $\mathbf{n}$ denotes the normal to the surface of the slotted waveguide. Fig. 1 illustrates the geometry. Placing the common centre of two orthogonal slots (so-called X-slots), each having a resonant length of $\lambda_0/2$, where λ_0 is the wavelength in free space, at the points x_1 or x_2, the wave propagating through the waveguide excites circularly polarised radiation in the *z*-direction. Like for dipole antennas, the slot width w is usually small
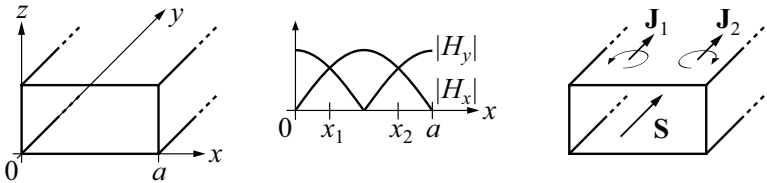

Fig. 1. Position of crossed orthogonal slots to produce circularly polarised radiation. The vector S denotes the power flow (Poynting's vector).

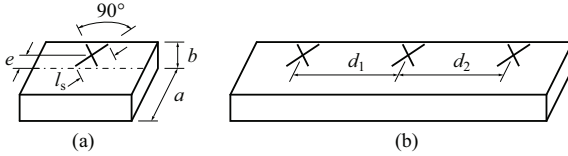**Fig. 2. (a) Single X-slot in the broad side of a waveguide broadside.**
(b) Extension to a three-element array.

compared to the length. The axial ratio reaches its minimum value of one, or 0 dB, at these coordinates.

To ensure a resonant length of each slot without cutting the sidewall of the waveguide, their orientation should be titled with respect to the y-axis by ±45 degrees, as indicated by Fig. 2.

For an ideal waveguide (perfect electric conductor) with standard dimensions (WR 42 at 20 GHz), according to numerical simulations of the antenna structure in Fig. 2 (a) with CST Microwave Studio [7], with $l_s=0.96$ $\lambda_0/2$ and $e=0.2521 \cdot a$, a single X-slot yields a radiation efficiency (waveguide input port to farfield) of $\eta=0.82$, a reflection coefficient of $S_{11}=$-22.3 dB, and a transmission coefficient $S_{21}=$-7.5 dB between the input and output ports of the waveguide. The antenna gain in main direction is $G=5.65$ dBi.

The simplest way to achieve a higher gain would intentionally be to form an array of multiple X-slots along the waveguide (Fig. 2 (b)). However, due to the propagation of the exciting wave, the phase differences due to the excitation currents and the geometrical placements of the X-slots have to be taken into account. The array pattern for an arrangement of N X-slots is given by

$$G_a(\mathbf{u}) = \sum_{i=0}^{N-1} \underbrace{a_i e^{-j2\pi\frac{D_i}{\lambda_g}}}_{\text{excitation}} \underbrace{e^{j2\pi\frac{D_i}{\lambda_0}\mathbf{d}\cdot\mathbf{u}}}_{\text{placement}} \quad , \text{ where } D_\zeta = \begin{cases} 0 & , \zeta = 0 \\ \sum_{i=1}^{\zeta} d_i & , \zeta > 0 \end{cases}, \tag{5}$$

where $\mathbf{u}$ describes the direction of propagation of the radiation, and $\mathbf{d}$ is the vector along the array [8]. The parameters a_i and d_i are $2N$-1 arbitrarily set variables which can be adjusted to optimise the radiation performance; a_i is a measure of the amount of power transmitted by the i-th X-slot, and d_i defines the distance to the previous pair of slots (see Fig. 2).

In many designs, equi-phase stimulation of all X-slots is assumed (i.e., in the excitation part of eq.). This can be achieved by placing the X-slots in a distance of $d_i = \lambda_g$ to each other. In a commonly air-filled waveguide, the guided wavelength λ_g is greater than $\lambda_0/2$; as a result, grating lobes occur in the radiation pattern. Further examination reveals that the radiated fields of all individual X-slots interfere constructively exactly at the propagation direction at which

$$-2\pi\frac{D_i}{\lambda_g} + 2\pi\frac{D_i}{\lambda_0}\mathbf{d}\cdot\mathbf{u} = -2\pi\frac{D_i}{\lambda_g} + 2\pi\frac{D_i}{\lambda_0}\sin(\theta) \overset{!}{=} 0 \tag{6}$$

holds or, in other words, where the complementary angle to the angle between $\mathbf{d}$ and $\mathbf{u}$ equals

$$\theta_{1,2} = \arcsin\left(\frac{\lambda_0}{\lambda_g}\right). \tag{7}$$

The subscripts 1 and 2 denote the two solutions of eq. (7) in the range $0 \leq \theta \leq 2\pi$. As a result, it is not possible to avoid the grating lobes through any slot displacements. Due to that fact, the distance between all slots is chosen $d_i = \lambda_g$ for all slots.

The amount of power radiated by each X-slot can be controlled by adjusting the slot length. A maximum is reached if the slots are made resonant, which means $l_s = 0.96\,\lambda_0/2$. To reduce the side lobe level, a_i should be symmetrically tapered along the waveguide. This means that the central elements radiate the greatest amount of power, their nearest neighbours a somewhat smaller part, and so on. Translating this approach into a design rule means that the slot lengths must be adjusted more and more closely
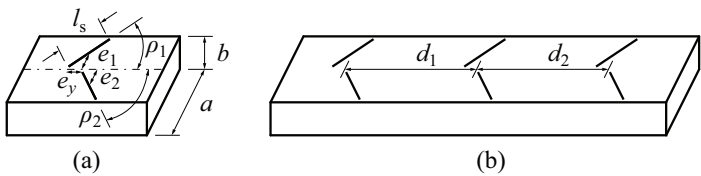

Fig. 3. (a) Single inclined slot pair antenna in a waveguide broadside.
(b) Extension to a three-element antenna.

to the resonant length along the direction of propagation in the exciting waveguide. Therefore the last X-slot has to be the shortest or the longest one.

B. Inclined-slots antenna

An alternative to obtain a circularly polarised radiation in z-direction is to cut two non-crossing, closely-spaced, inclined slots in the broadside of the waveguide, as illustrated by Fig. 3. Each slot has the resonant length of $\lambda_0/2$, a width w small compared to the free-space wavelength, is inclined with respect to the waveguide axis at an angle $\varrho_{1,2}$, and has an offset of $e_{1,2}$. The spacing between the centres of the slots is given by e_y. These parameters can be varied to achieve the desired quality of polarisation and amplitude of the radiating field. For the sake of simplicity, the angles $\varrho_{1,2}$ were set to ± 45 degrees and both offsets $e_{1,2}$ are assumed to be equal. Starting with the arrangement of crossed slots for circular polarisation, the parameters were iteratively optimised by parameter sweeps.

The numerical simulations of a single slot pair in an ideal waveguide yield a reflection coefficient of S_{11}=-11.7 dB and a transmission coefficient of S_{21}=-6 dB between the two waveguide ports. It is apparent that the inclined slots possess higher mismatch in comparison to the X-slots. Accordingly, a lower efficiency of η=0.66 was simulated. The antenna gain in the main direction reaches G=4.8 dBi. In order to increase the antenna gain further, an extension towards an array is appropriate. Due to the non-resonant slots, the radiated power of each slot pair depends on the slot length and should also be varied between all pairs, to obtain an amplitude tapering along the linear slot array.

III.   Implementation

In this section, the implementation of both techniques discussed above into four-element arrays is described. The waveguide structure is realised by a U-shaped profile milled in solid brass (see Fig. 4). The open side of the U-profile is covered with a dielectric substrate, which is copper-plated at the bottom side (Rogers Ro4003C [9]) and solder-connected to the brass profile at the edges. The radiating slots are etched into the Rogers material.
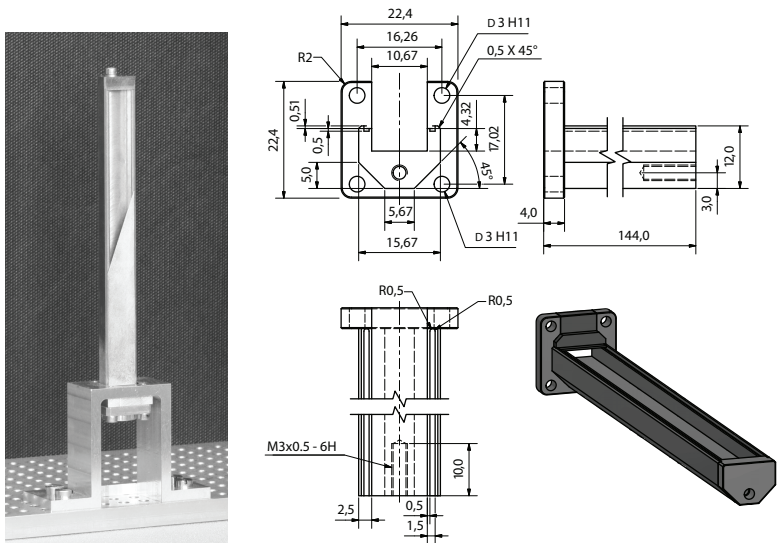
Fig. 4. Photograph (left-hand part) and technical drawing (right-hand part, with millimetre dimensioning) of the waveguide structure.

At one end of this sheet, a WR42 waveguide flange is placed, to enable the use of standard waveguide components for the antenna feed. This technique facilitates a fast and precise method to fabricate slotted waveguide antennas, especially for laboratory versions. For measurements of the radiation pattern, a dedicated mounting was fabricated.

The dielectric substrate of the covering printed circuit board (PCB) changes the effective permittivity near the slots. This requires a shortening of all slots approximately by $\sqrt{\varepsilon_{\text{eff}}}$, in order to keep the desired radiation scheme. As another consequence, it is possible to realise non-resonant behaviour even with longer slots. This principle was applied to the design of the inclined-slots antenna.

Table 1 summarises the most convenient dimensions for both types of antennas. These were found by parametric full-wave simulations with CST Microwave Studio. For the crossed-slot antenna, a single X-slot was simulated with a parametric slot-length. The transmission between input and ouput ports of the waveguide, and the farfield were examined for each

length step.

In order to keep the side lobe levels low, the coefficients of eq. (5) were set according to:

$$a_1 = 0.4 \cdot a_2 = 0.4 \cdot a_3 = a_4. \tag{8}$$

Slots in a waveguide can be considered as a discontinuity which adds a phase shift to the transmitted field. To eliminate this effect, the slot distances were adapted in both designs, yielding a corrected main beam direction of zero degree elevation.

To determine the optimum dimensions of the inclined slots, a similar iterative strategy was applied. Starting from a single slot pair, initially designed with $e_1 = e_2 = 0.252 \cdot a$ and $e_y = 0$, these values were optimised with respect to the geometric boundary conditions, until the maximum possible polarisation purity was reached. In next the step, the four-element array was adapted to these values and the length of each slot pair was tuned to control the amount of radiated power, to reduce the side lobe level.

IV. Simulation results

The numerical simulations of both structures enable a comparison of their performance and, hence, their suitability for mobile satellite communications. Efficiency, gain, and polarisation purity are decisive for such applications. The cross polarisation discrimination (XPD) G_{xpd} is a measure for the polarisation purity. For left-handed circular polarisation (LHCP) it is defined as

$$G_{xpd} \text{ [dB]} = G_{co} \text{ [dBi]} - G_{cross} \text{ [dBi]} = G_{left} \text{ [dBi]} - G_{right} \text{ [dBi]}, \tag{9}$$

where G_{left} and G_{right} are the antenna gains for right- and left-handed polarisations in main direction [10]. Fig. 5 and Fig. 6 show vertical and horizontal cuts through the farfield gain patterns. The expected grating lobe at 45.4

	$e = e_1 = e_2$	e_y	d	l_{S1}	l_{S2}	l_{S3}	l_{S4}	w
Crossed slots	$0.252 \cdot a$	–	$0.88 \cdot \lambda_g$	$0.339 \cdot \lambda_0$	$0.351 \cdot \lambda_0$	$0.358 \cdot \lambda_0$	$0.378 \cdot \lambda_0$	$0.013 \cdot \lambda_0$
Inclined slots	$0.178 \cdot a$	$0.152 \cdot \lambda_g$	$1.10 \cdot \lambda_g$	$0.380 \cdot \lambda_0$	$0.365 \cdot \lambda_0$	$0.354 \cdot \lambda_0$	$0.347 \cdot \lambda_0$	$0.033 \cdot \lambda_0$

Table 1. Most convenient geometrical dimensions for both antennas (in millimetres).
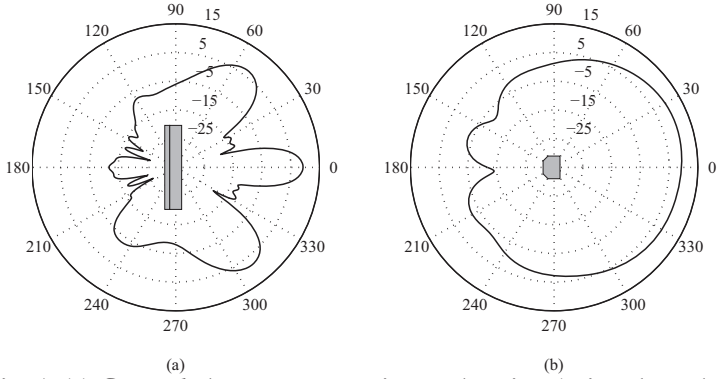
Fig. 5. (a) Crossed-slots antenna, gain vs. elevation (azimuth angle of 0 degree) in dBi. (b) Crossed-slots antenna, gain vs. azimuth (elevation angle of 0 degree) in dBi. The position of the waveguides is indicated by the grey shapes.

degree is clearly noticeable in panel (a) of both figures. The 3-dB beamwidth reaches 12.7 degrees in elevation for the X-slots, and 9.5 degrees for the inclined slots. Furthermore, asymmetries are recognisable in the (b) panels, especially in Fig. 6. The highest gain appears at about 19 to 20 degrees in azimuth; the 3-dB beamwidth is 105.6 degrees for the crossed slots and 95.6 degrees for the inclined slots. Because of the wider spatial distribution of the radiated field in the X-slot design, the crossed-slots antenna yields a lower gain in the main direction. However, the simulated gain values are as expected for four-element arrays of the different radiating elements. To obtain a higher efficiency, the transmission coefficient of both antennas could be reduced, e.g., by increasing the number of slots. The lower reflection coefficient of the crossed-slots antenna was expected because of a lower S_{11} value of the single X-slot anticipated in section II. Table 2 eventually compiles selected results for the crossed and inclined

	S_{11} [dB]	S_{21} [dB]	η	G [dBi]	G_{xpd} [dB]
Crossed slots	−25.9	−10	0.83	9.3	−21.6
Inclined slots	−8.9	−13.7	0.79	10.3	−10.7

Table 2. Selected results of the numerical simulations for 20 GHz, with the waveguide excited at port 1.
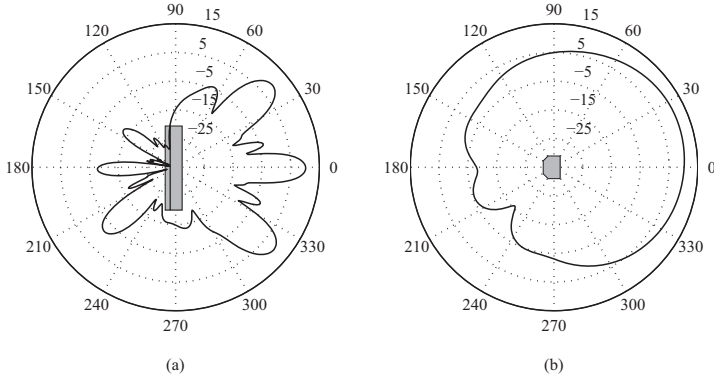
Fig. 6. (a) Inclined-slots antenna, gain vs. elevation (azimuth angle of 0 degree) in dBi. (b) Inclined-slots antenna, gain vs. azimuth (elevation angle of 0 degree) in dBi. The position of the waveguides is indicated by the grey shapes.

slots in main direction (zero degree elevation and azimuth angle) for a frequency of 20 GHz.

V. Conclusions and Outlook

In this contribution, two low-profile slotted-waveguide antennas were designed and examined by simulations. By placing and dimensioning crossed or inclined slots along the broad side of a rectangular waveguide, circularly polarised antennas were developed. For the X-slots, high cross polarisation discrimination and a low reflection coefficient could be achieved. The inclined-slots antenna reached a slightly higher gain in the main direction. Both antennas can be scaled easily to a two-dimensional receiving antenna array for mobile satellite communication in Ka-band.

Future activities include experimental confirmation of the simulated parameters. In addition, techniques to reduce the grating lobes need to be developed further, and proper trade-offs with radiation efficiency and gain identified, in order to use circularly polarised slotted-waveguide antennas also for transmission in the corresponding return channel at 30 GHz [11].

References

[1] J. Kemp, "Wave guides in electrical communication," Journal of the Institution of Electrical Engineers - Part III: Communication Engineering, including the Proceedings of the Wireless Section of the Institution, vol. 90, no. 11, pp. 90-114, Sep. 1943.

[2] S. R. Rengarajan, L. Josefsson, R. Petersson, "Recent developments in broad walls slots in rectangular waveguides for array applications," Seventh International Conference on Antennas and Propagation, vol. 2, pp. 729-731, 15-18 Apr. 1991.

[3] A. Simmons, "Circularly polarized slot radiators," IRE Transactions on Antennas and Propagation, vol. 5, no. 1, pp. 31-36, Jan. 1957.

[4] A. Seaton, G. Carnegis, "A novel circularly polarized planar array for surveyor," IRE International Convention Record, vol. 11, pp. 2- 9, Mar. 1963.

[5] G. Montisci, M. Musa, G. Mazzarella, "Waveguide slot antennas for circularly polarized radiated field," IEEE Transactions on Antennas and Propagation, vol. 52, no. 2, pp. 619-623, Feb. 2004.

[6] H. G. Booker, "Slot aerials and their relation to complementary wire aerials (Babinet's principle)," Journal of the Institution of Electrical Engineers - Part IIIA: Radiolocation, vol. 93, no. 4, pp. 620-626, 1946.

[7] (2010). 3D EM Field Simulation - CST Computer Simulation Technology [Online]. Available: http://www.cst.com

[8] R. S. Elliott, Antenna Theory and Design. Hoboken, NJ: Wiley-IEEE Press, 2003.

[9] (2010). Rogers Corporation [Online]. Available: http://www.rogerscorp.com

[10] P. Watson, S. Ghobrial, "Off-axis polarization characteristics of Cassegrainian and front-fed paraboloidal antennas," IEEE Transactions on Antennas and Propagation, vol. 20, no. 6, pp. 691- 698, Nov. 1972.

[11] Harmonized EN for Satellite Interactive Terminals (SIT) and Satellite User Terminals (SUT) transmitting towards satellites in geostationary orbit in the 29,5 GHz to 30,0 GHz frequency bands covering essential requirements under article 3.2 of the R&TTE Directive, ETSI EN 301 459, 2007.

Methods of increasing efficiency of wireless power transmission system

D.S. Kozlov, M.A. Odit, D.A. Sokolov, O.G. Vendik

Microwave Microelectronics Laboratory, St. Petersburg Electrotechnical University "LETI", 5 Prof. Popov st., 197376 St. Petersburg, Russia

Abstract

Scientists are interested in wireless power transmission for a long time. Nowadays great efforts in development of wireless power transmission are applied all around the world. An application of wireless systems for powering electronic devices is an emerging technology that can offer a lot of benefits in the nearest future. It can make everyday products (LAN devices, cell phones, laptop computers and other portable electronics) more convenient and reliable. The main problem limiting a wide application of wireless electricity is an insufficient efficiency of wireless power transfer. That is why we consider different methods of increasing efficiency of these systems.

As a wireless power transmission system two metal loops are considered. The energy transfer is provided by the quasistatic magnetic coupling between the inductive coils. It was proposed to update the structure of the magnetic field between two loops for increasing efficiency of the system. It was achieved by application of Artificial Magnetic Wall (AMW). A theoretical calculation has shown that application of the AMW increased the efficiency by a factor of two. After that the electromagnetic simulation was produced. Obtained results confirmed our theoretical assumption about appropriateness of AMW application in the wireless power transmission system.

Keywords —**wireless power transmission, quasistatic magnetic field, optimized efficiency, artificial magnetic wall.**

I. Introduction

Of late years wireless power transmission systems are highly popular whereas these systems are beginning to get a practical application. And many companies are developing such systems. So for example company Intel had demonstrated its wireless power transmission system (Fig. 1) at the exhibition in 2008 [1].

Wireless energy transfer is most effective at high frequencies. But it's not acceptable to use such systems in everyday life. That's why it was considered the system operating on the frequency of $f_0 = 13.56$ MHz. As generally known the frequency 13.56 MHz is the standardized frequency actively using in high frequency technology and RFID-systems. As we know wireless systems are usually characterized by a low efficiency of power transfer. Therefore the design was improved for increasing efficiency of these systems. The Artificial Magnetic Wall (AMW) was used in the construction of the transfer system.

II. The wireless transfer system

Considered wireless power transmission system (Fig. 2) is based on the system described in the article [2]. It consists of two metal loops with currents. The distance between them is equal to s and the radii of both loops are R. The energy transfer is provided by the quasistatic magnetic coupling
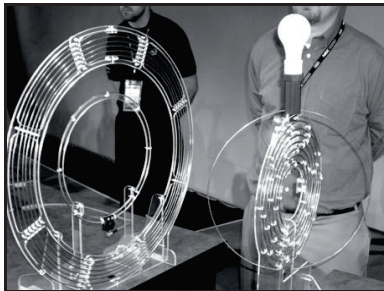
Fig. 1. Intel wireless power transmission system.
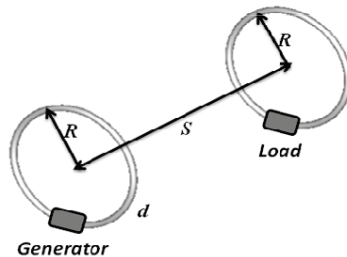
Fig. 2. The wireless transfer system with R - radius of the loop, d - diameter cross-section of the loop and s - distance between loops.
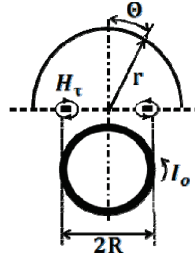
Fig. 3. The loop in spherical coordinate system.

between the inductive coils.

Let's consider the distribution of the magnetic field around a transmitting loop (Fig. 3). Components of the magnetic intensity in the spherical coordinate system are determined by the following equations [3].

$$H_r = i\frac{ka^2 I_o \cos\Theta}{2r^2}[1 + \frac{1}{ikr}]e^{-ikr} \tag{1}$$

$$H_\Theta = -\frac{(ka)^2 I_o \sin\Theta}{4r}[1 + \frac{1}{ikr} - \frac{1}{(kr)^2}]e^{-ikr} \tag{2}$$

$$H_\varphi = 0 \tag{3}$$

In the near-field zone ($a < r << \lambda$) components of the magnetic intensity are determined by these simplified equations:

$$H_r = \frac{a^2 I_o \cos\Theta}{2r^3} \tag{4}$$

$$H_\Theta = \frac{a^2 I_o \sin\Theta}{4r^3} \tag{5}$$

$$H_\varphi = 0 \tag{6}$$

In this case the magnetic field can be considered as quasistatic.

The efficiency of energy transfer can be evaluated using the coupling coefficient, which is read as:

$$k = \frac{M}{\sqrt{L_1 L_2}} \tag{7}$$
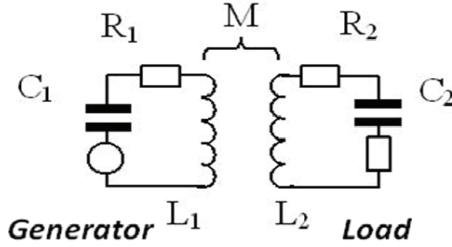
Fig. 4. Equivalent diagram of the system.

where M is the mutual inductance between two loops (8) and L1, L2 is the inductance of the loops (9).

$$M = \mu_o \frac{\pi}{2} \frac{(R_1 R_2)^2}{s^3} \qquad (8)$$

$$L_1 = L_2 = L = \mu_0 R[\ln \frac{16R}{d} - 2] \qquad (9)$$

Our wireless power transmission system is equivalent to the electrical circuit if the capacitors are included in the loops (Fig. 4).

On solution to the system of Kirchhoff equations we can calculate an efficiency of the system. At the resonant frequency it is determined by the expression (10) if the load resistance provides the maximum of efficiency.

$$\eta = \frac{1}{1 + \frac{2}{k_{eff}^2}(1 + \sqrt{1 + k_{eff}^2})} \qquad (10)$$

where $k_{eff} = k \cdot Q$ is an effective coupling coefficient, Q is a quality-factor of the loop.

Thus the efficiency of the system can be improved by increasing of the coupling coefficient or the Q-factor of the loop. It was suggested that the coupling coefficient can be increased by upgrading the structure of the magnetic field near the loop. It can be achieved by application of the artificial magnetic wall in the system of energy transfer.
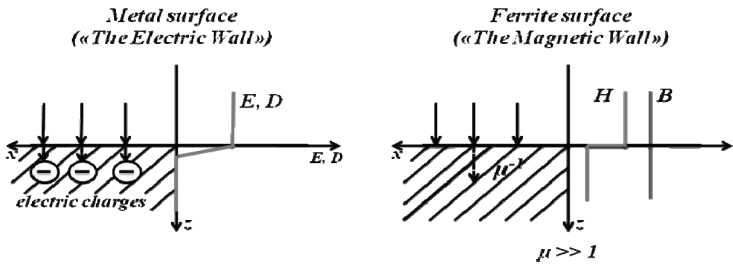
Fig. 5. Metal and ferrite surfaces.

III. Magnetic Wall

The magnetic wall is the surface where the tangent component of the magnetic field is equal to zero and magnetic field lines are terminated on it. The magnetic wall is dual with respect to the electric wall. However there is important fundamental difference. The main distinction is caused by the absence of magnetic charges in contrast to the existence of electrical charges in nature. Therefore magnetic field lines don't terminate on the magnetic wall. So the artificial magnetic wall can be realized by using materials with high value of magnetic permeability μ (for example: ferrite). The magnetic intensity H changes abruptly in μ times (Fig. 5). The structure of the magnetic field near a layer of ferrite is similar to the structure of the magnetic field near a perfect magnetic wall.

$$I = \oint H dl \tag{11}$$

$$\Phi = \mu_o \int H dS \tag{12}$$

$$L = \frac{\Phi}{I} \tag{13}$$
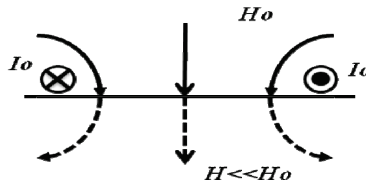
Fig. 6. The surface of the Magnetic Wall.
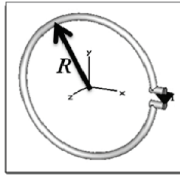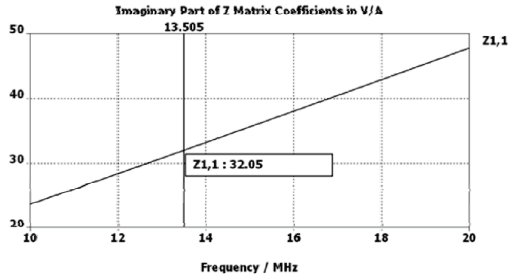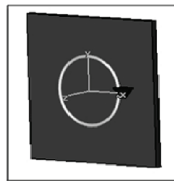
R = 10 cm
d = 1 cm
f = 13.5 MHz

Fig. 7. The single loop.

Now let's consider in more detail an application of the magnetic wall in the energy transfer system (Fig. 6). Magnetic field lines are terminated on a magnetic wall's surface. Thus the contour of integration is two times smaller (11). So the value of magnetic intensity is two times greater. Consequently values of magnetic flux and inductance of the loop are two times greater as well (12), (13). Simultaneously the value of mutual inductance is four times greater. Finally the coupling coefficient is doubled in theory (7).

IV. Electromagnetic simulation

In this section, results of electromagnetic simulations are presented. All results have been obtained with CST Microwave Studio.
At first the single transmitting loop was considered. The radius of the loop is 10cm. The value of the inductive reactance obtained in simulation is

R = 10 cm
d = 1 cm
f = 13,5 MHz
μ_ferrite = 300
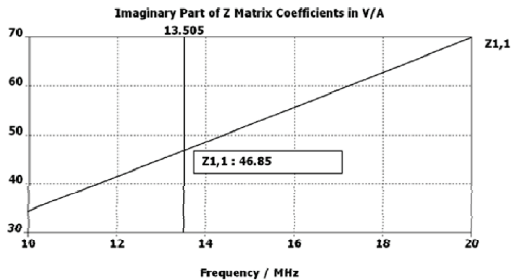
Fig. 8. The single loop located on the ferrite layer.

56

Fig. 9. The distribution of the magnetic field.

R = 10 см
d = 1 см
f = 13,5 МГц
s = 50 см
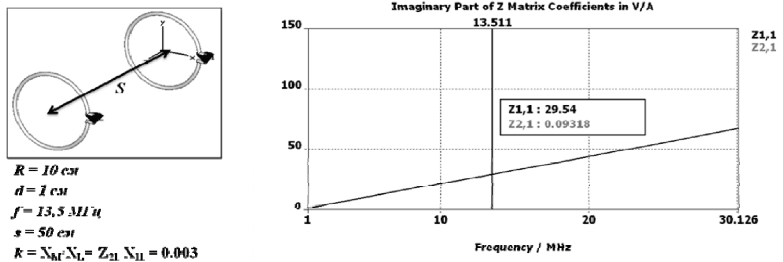k = $X_M \cdot X_L = Z_{21} \cdot X_{11} = 0.003$
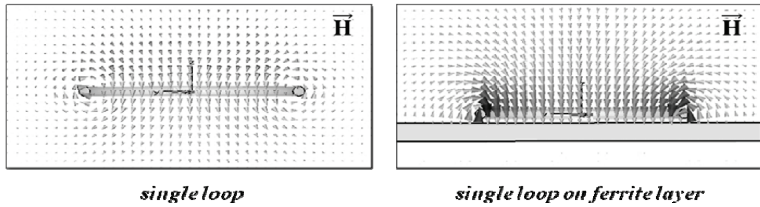
Fig. 10. Ttransmitting and receiving loops.

equal to 32 Ohm at the frequency 13.5MHz (Fig. 7). Theoretically calculated value is equal to 33 Ohm (9).

In the case of transmitting loop located on the ferrite layer, the value of the inductive reactance obtained in simulation is equal to 47 Ohm (Fig. 8). Magnetic permeability of ferrite is equal to 300. The thickness of the layer is 2 cm and the loop is located at a height of 0.5 cm over the ferrite sur-
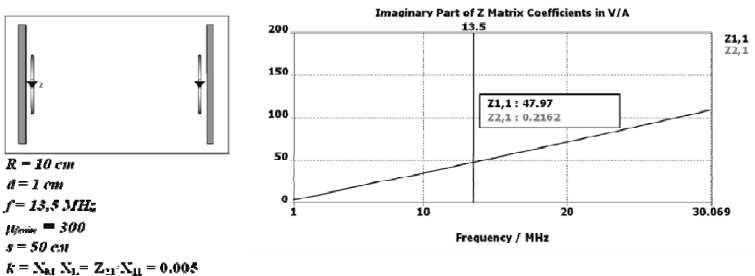

R = 10 cm
d = 1 cm
f = 13,5 MHz
$\mu_{ferrite}$ = 300
s = 50 см
k = $X_M \cdot X_L = Z_{21} \cdot X_{11} = 0.005$

Fig. 11. Ttransmitting and receiving loops located on the ferrite layers.
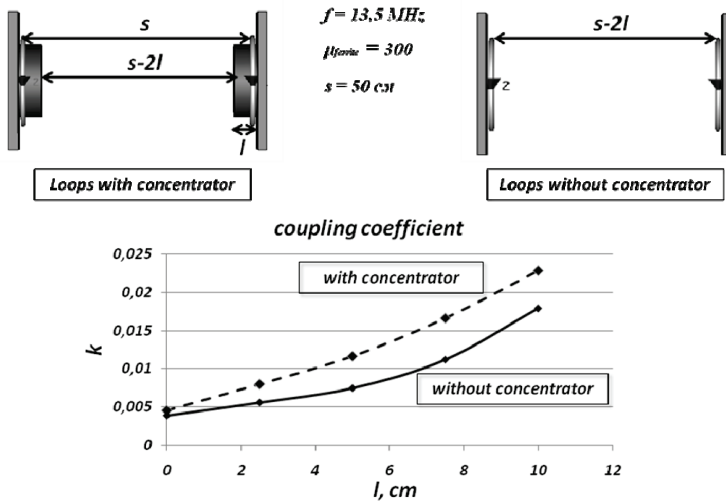
Fig. 12. Ferrite cylindrical concentrator.

face. It confirms the assumption that the magnetic wall increases magnetic intensity and inductance of the loop.

The figure 9 shows the distribution of the magnetic field in both cases. It distinctly seen that magnetic field lines are terminated on the ferrite surface and the intensity of the field is considerably greater. Thus the ferrite layer is similar in properties to the magnetic wall. Therewith the layer of ferrite can be used as a shield for the magnetic field.

In the fig. 10, the structure consists of transmitting and receiving loops is shown. The distance between them is $s = 50$ cm. The value of the coupling coefficient obtained by simulation is 0.003. In the case of two loops located above ferrite layers coupling coefficient is 0.005 (Fig. 11). This value is greater than previous one about two times.

Moreover the coupling coefficient between two loops can be increased by concentration of the magnetic field. For example a small ferrite cylindrical concentrator situated above the surface of the ferrite layer can be used. The radius of the cylinder a is 8 cm and the length is l.

The figure 12 shows the relation of the coupling coefficient between two loops on the cylinder length -l. The distance between them is $s = 50$ cm.

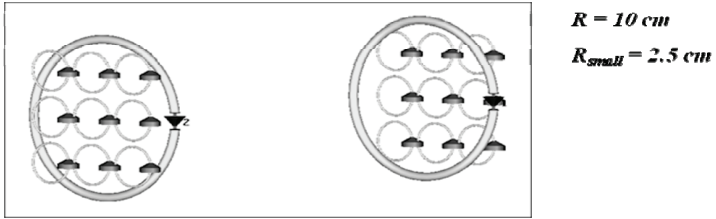R = 10 cm
R_small = 2.5 cm

Fig. 13. Two loops with layers of 9 small resonant loops.

On the same diagram, the relation of the coupling coefficient between two loops located above the ferrite layers is shown. In this case the actual distance between the loops is s-$2l$. As we see, the application of the ferrite concentrator increases the coupling coefficient.

Also the system including the layer of 9 small metal loops was simulated (Fig. 13). This layer is located at the distance of 1 cm from main loop. The radius of big loop is 10 cm and the radius of small loop is 2.5 cm. All small loops are loaded with capacitors.

The coupling coefficient was calculated for the system shown at the fig. 13. The distance between big loops is 50 cm.
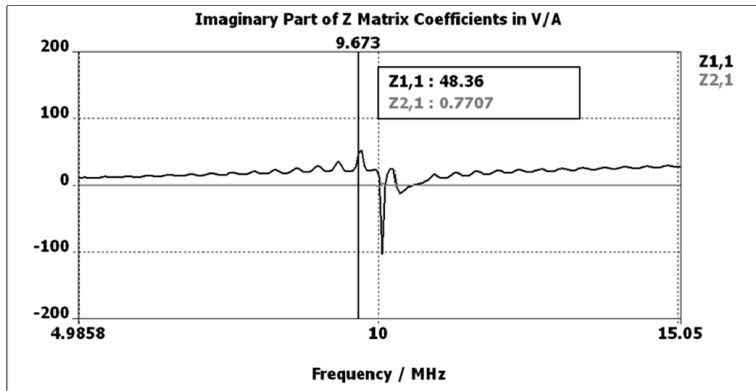
$k = X_M \cdot X_L = Z_{21} \cdot X_{11} = 0.016$

Fig. 14. The coupling coefficient between two big loops.

As we see the coupling coefficient is equal to 0.014 at the resonant frequency of the small loops. But at this frequency the resistance of the big loop drastically increases. As a result the most part of the active-power transfer is dissipated in small loops and the efficiency of the system reduces.

V. Conclusion

It has been shown that application of the magnetic wall increases the efficiency of the wireless power transmission system. A ferrite layer can be used as an artificial magnetic wall. Also it exhibits shielding properties.
The distribution of the magnetic field around 9 resonant loops is similar to the distribution of the magnetic field near the magnetic wall. But power transmission in this system can be effective if the resistance of the big loop will be decreased.

References
[1]   Intel Wireless Power Transmission, http://www.technovelgy.com/ct/Science-Fiction-News.asp?NewsNum=1836

[2]   A. Kurs, A. Karalis, R. Moffatt, J.D. Joannopoulos, P. Fisher, M. Sobjacic, "Wireless power transfer via strongly coupled magnetic resonances" Science, vol. 317, 2007, pp. 83–86.

[3]   C. A. Balanis, Advanced Engineering Electromagnetics (Wiley, New York, 1989).

Novel „Matreshka"-Type LTCC Resonators Based on Nested Capacitively Loaded Cavities for Dual-Band Filtering Applications

Viacheslav Turgaliev and Dmitry Kholodnyak

Microwave Microelectronics Laboratory, Department of Microelectronics & Radio Engineering, St. Petersburg Electrotechnical University "LETI", 5 Prof. Popov st., 197376 St. Petersburg, Russia

Abstract

Using capacitively loaded LTCC cavities allows designing small-size and low-loss bandpass filters for the low part of the microwave region. The size of a highly loaded LTCC cavity can be as low as one eighth of the guided wavelength and even smaller while the Q-factor of such a miniature resonator still remains much higher as compared to a quasi-lumped-element LTCC resonator. In this paper novel LTCC structures of miniature dual-mode resonators based on two capacitively loaded cavities, which are nested one into another like a set of the well-known traditional Russian dolls „matreshka" are proposed. Design of these novel dual-mode resonators, their simulated characteristics, and results of experimental investigations are presented. The dual-mode „matreshka"-type resonators suit well to design of miniature low-loss LTCC filters for dual-band applications. A 3-pole dual-band filter with the passbands of 698-798 MHz and 1710-1788 MHz was designed. The entire size of the filter is as small as one twelfth of the guided wavelength at the central frequency of the ower passband. According to the results of the 3D electromagnetic simulation, the filter is characterized by low insertion loss that does not exceed 1.4 dB and 2.1 dB in the lower and higher passbands, correspondingly.

Keywords — **Dual-mode resonator, dual-band filter, loaded cavity, high Q-factor, Low Temperature Co-fired Ceramics (LTCC).**

I. Introduction

In order to provide a compact size, the bandpass filters for the L- and S-bands implemented by means of the multilayer Low Temperature Co-fired Ceramics (LTCC) technology are commonly based on quasi-lumped elements. These filters exhibit a remarkable insertion loss due to a very limited Q-factor of the quasi-lumped-element resonators.

On the other hand, small-size and low-loss LTCC filters can be designed using capacitively loaded cavities [1]. It is well known that the capacitive loading decreases the cavity size while the Q-factor is also decreased. There is a trade-off between the size and the Q-factor. However, since the Q-factor of the quasi-lumped-element LTCC resonators is at least 5-10 times smaller compared with the unloaded cavity, an efficient cavity downsizing can be achieved. The size of a highly loaded LTCC cavity can be as low as one eighth of the guided wavelength (λ_g) and even smaller while its Q-factor still remains much higher than that of a quasi-lumped-element LTCC resonator [1]. The unloaded Q-factor of about 200 is demonstrated in this paper by the results of experimental investigation of the LTCC cavity having the approximate size of $\lambda_g/8$.

Novel miniature dual-mode LTCC resonators based on the capacitively loaded cavities, which are nested one into another like a set of the well-known traditional Russian dolls „matreshka", are proposed in this paper. These resonators are well suited to design of compact low-loss dual-band filters because nesting the cavities allows an efficient decreasing of the area occupied by the filter. Design of the 3-pole dual-band filter with the passbands of 698-798 MHz and 1710-1788 MHz is presented to demonstrate a high potential of the resonators proposed.

II. Investigation of LTCC capacitively loaded cavity

A structure of square-shape cavity filled with LTCC and loaded by a conductive post with a capacitive plate at one end is shown in Fig. 1-a. In order to demonstrate the internal structure of the resonator, the middle part of the top ground plane is not shown in the figure. Sidewalls and the square post are formed by rows of stacked via holes. The resonator is connected

with external circuits by inductive coupling elements. Input and output co-planar feed lines are situated on the top of the LTCC structure.

Due to technological reasons, the height of the LTCC structure is limited to a few millimeters. Such a resonator operates on TM_{110} mode [2]. Since the post inductance L is rather low, a high capacitive loading is required for an efficient size reduction. Meanwhile, the resonator size is determined by the area of the capacitive plate that can be decreased by using the upper LTCC layer as thin as possible.

In the highly loaded cavity, the electric field is concentrated between the capacitive plate and the top of the cavity. The resonant frequency is reduced significantly with increasing capacitance. However, the magnetic field distribution remains relatively unchanged and consequently the metal loss, which is associated with the tangential magnetic field on metal surfaces, does not change significantly. As a result, the unloaded Q-factor of the resonator does not drop as quickly as the resonant frequency does [3]. This gives a possibility to design highly loaded LTCC cavities, which are comparable in size with quasi-lumped-element LTCC resonators but have the unloaded Q-factor of 2-3 times higher [1].

The capacitively loaded LTCC cavity shown in Fig. 1-a was designed with the aid of Ansoft HFSS 3D electromagnetic field solver. The resonator was embedded into nine layers of DuPont Green TapeTM 951 LTCC (ε_r = 7.8).
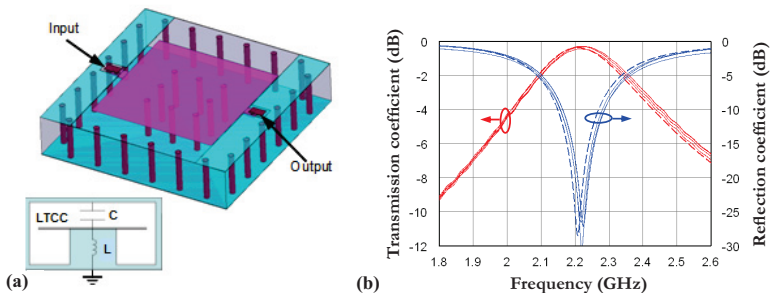

Fig. 1. Capacitively loaded LTCC cavity: (a) structure and (b) measured characteristics of four experimental samples (solid lines) and those predicted by 3D electromagnetic simulation (dashed lines). Middle part of the top ground plane is not shown to demonstrate the internal structure.

Six of them have the thickness of 210 m after sintering, two layers have the thickness of 42 μm, and one layer is 95 μm thick. Thus, the total height of the LTCC structure is about 1.44 mm. The internal size of the cavity with the resonant frequency of 2220 MHz is as small as 6 mm × 6 mm (~$\lambda_g/8$). The post has the size of 2 mm × 2 mm with the capacitive plate of 4.4 mm × 4.4 mm.

The LTCC structure was manufactured using DuPont 6148 Ag co-fireable conductor paste and DuPont 6141 AgPd cofireable via fill paste. Experimental investigation of the resonator characteristics was carried out using a vector network analyzer and a probe station with coplanar probes for on-wafer measurements. A TRL calibration technique was used. Four test samples of the resonator were fabricated and measured. Experimentally obtained characteristics of all four samples are plotted in Fig. 1-b in comparison with a performance predicted by the 3D electromagnetic simulation. A good agreement between the measured and simulated data is observed as well as a very good repeatability of the characteristics measured for different samples. The estimated unloaded Q-factor of this resonator is about 200.

III. Dual-mode „matreshka"-type LTCC resonators on nested capacitively loaded cavities

The capacitively loaded cavities with different resonant frequencies can be nested one into another like the traditional Russian dolls „matreshka" (Fig. 2). The simplest structure of two nested capacitively loaded LTCC cavities is shown in Fig. 2-a. In this case, the external surface of the internal cavity serves as the capacitive loading for the outer cavity. Such a configuration allows decreasing the area occupied by two cavities. However, there is a trade-off between the area reduction and height increasing. An equivalent diagram of two nested cavities structure is presented in Fig. 2-b. Such a structure operates as a dual-mode resonator providing a transmission zero between two resonances. It is important to note that the resonant frequencies can be chosen arbitrary.

Fig. 2-c presents a modified structure of the dual-mode resonator. The above mentioned two nested cavities are surrounded by a LTCC shell and
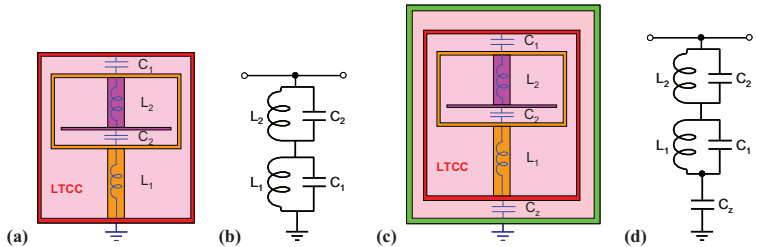
Fig. 2. Dual-mode „matreshka"-type LTCC resonators: schematic representation (a) and equivalent diagram (b) of two nested capacitively loaded cavities; schematic representation (c) and equivalent diagram (d) of the modified resonator providing an additional transmission zero.

a grounded conductive box to provide a capacitance to the ground. An equivalent diagram of this modified structure is shown in Fig. 2-d. The presence of the capacitance C_z results in appearance of an additional transmission zero below the resonant frequencies.

A practical implementation of the dual-mode „matreshka"-type resonator by means of the LTCC technology is illustrated in Fig. 3. In order to demonstrate the inner structure of the resonator, a part of the stacked via holes, which are used as the side walls, and a part of the top ground plane are not shown in the figure. Though this generalized structure represents
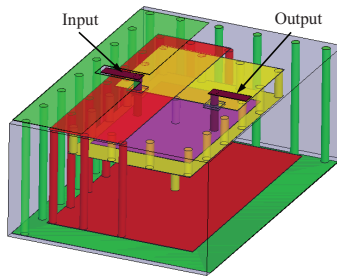

Fig. 3. 3D view of the generalized LTCC structure of the dual-mode „matreshka"-type resonator. A part of the stacked via holes used as the side walls and a part of the top ground plane are not shown to demonstrate the inner structure.
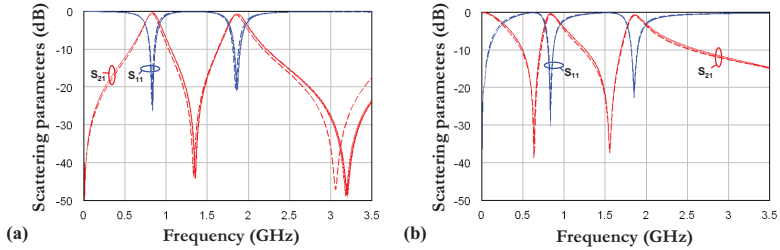
Fig. 4. Characteristics of the „matreshka"-type LTCC resonators obtained by 3D electromagnetic simulation (dashed lines) and by measurements of four experimental samples (solid lines): the dual-band resonator without an additional transmission zero (a) and the dualband resonator with an additional transmission zero (b).

the dual-mode resonator with an additional transmission zero (Fig. 2-c), it can be easily transformed to the resonator without transmission zero (Fig. 2-a) by introducing via holes between the larger cavity and the grounded box to short-circuit the capacitance C_z.

In order to demonstrate a feasibility of the design approach proposed, two miniature dual-mode resonators with and without an additional transmission zero were designed for the non-multiple resonant frequencies 748 MHz and 1848 MHz on the base of the LTCC structure shown in Fig. 3. The entire size of the each resonator embedded in 16 layers of DuPont Green TapeTM 951 is 7.6 mm × 5.2 mm. The total height of the LTCC structure is 2.9 mm. These resonators were manufactured and experimen-
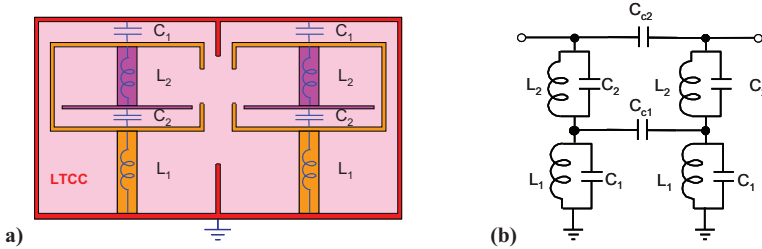

Fig. 5. Two coupled dual-mode „matreshka"-type LTCC resonators: schematic representation (a) and equivalent diagram (b).
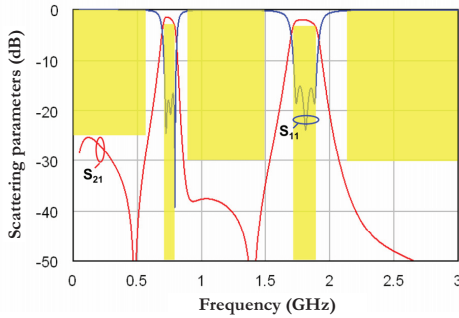
66

Fig. 6. Simulated characteristics of the three-pole dual-band LTCC filter based on „matreshka"-type nested cavities.

tally investigated. Measured characteristics of four experimental samples of each resonator are presented in Fig. 4 along with the results of the electromagnetic simulation in Ansoft HFSS. A very good repeatability for different samples and a good coincidence between the measured and simulated characteristics are observed for the both resonators.

IV. Dual-band LTCC filter design using the „matreshka"-type resonators

A coupling between two single-mode cavities is provided by an iris in the mutual side wall of the resonators [1]. Though such a coupling is generally mixed, electromagnetic simulations show that the main contribution is made by the electric field, i.e. the coupling is mainly the capacitive one. The coupling value depends on the iris size.

When using the dual-mode resonators based on two nested cavities, a coupling between the external cavities is realized in the same way as mentioned above while a coupling between the internal cavities is provided by two irises in their adjacent side walls as sketched in Fig. 5-a. In this case, the presence of the internal coupling increases the value of the external coupling that is to be corrected. An equivalent circuit of two coupled dual-mode „matreshka"-type resonators is depicted in Fig. 5-b.

The following example demonstrates a high potential of the „matreshka"-

type dual-mode resonators to the design of compact low-loss filters for dual-band applications. A three-pole LTCC filter with two passbands of 698–798 MHz and 1710–1788 MHz was designed using the structure of two nested capacitively loaded cavities with an additional transmission zero (Fig. 3). The entire size of the designed dual-band LTCC filter implemented on DuPont Green Tape™ 951 LTCC is 12 mm × 7.6 mm that corresponds to only $\lambda_g/12$ at the central frequency of the lower passband. This filter is characterized by a low insertion loss and a very good selectivity having very compact size (Fig. 6). According to the results of electromagnetic simulation, the insertion loss does not exceed, 1.4 dB and 2.1 dB in the lower and higher passbands, correspondingly.

V. Conclusion

Novel dual-mode resonators consisting of two nested capacitively loaded LTCC cavities have been proposed. The use of these „matreshka"-type resonators is very beneficial for the design of low-loss and small-size dual-passband filters because it allows an efficient decreasing of the area occupied by the filter. The feasibility of the design approach has been confirmed by the results of electromagnetic simulations and experimental investigations. The high-performance dual-band LTCC filter has been designed using the proposed „matreshka"-type resonators.

Acknowledgment

References

[1]   V. Turgaliev and D. Kholodnyak, „Miniaturized low-loss LTCC band pass filters on capacitively-loaded cavities“, ACTA Universitatis Ouluensis, Series C Technica, 2009, Vol. 323, pp. 85-92.

[2]   P. Ferrand, D. Baillargeat, S. Verdeyme, J. Puech, M. Lah, and T. Jaakola, „LTCC reducedsize bandpass filters based on capacitively loaded cavities for Q band application“, IEEE MTT-S Int. Microwave Symp. Dig., 2005, pp. 1789-1792.

[3]   X. Gong, A. Margomenos, B. Liu, W.J. Chappell, and L.P.B. Katehi, „High-Q evanescent-mode filters using silicon micromachining and polymer stereolithography (SL) processing“, IEEE MTT-S Int. Microwave Symp. Dig., 2004, pp. 433-436.

Design of Miniature Microwave Phase Shifters Using Hybrid Integrated Circuits Technology and Surface Mounted Devices

E.Yu. Zameshaeva[#1], P.A. Turalchuk[#1], D.V. Kholodnyak[#1], I.B. Vendik[#1], and M.D. Parnes[#2]

[#1] *Dept. of Microelectronics and Radio Engineering, St. Petersburg Electrotechnical University "LETI" / 5, Prof. Popov Str., St. Petersburg, Russia*
[#2] *JSC Rezonance / 27, Engels Ave., St. Petersburg, Russia*

Abstract

The design of two miniature phase shifters using low-cost fabrication technology of hybrid microwave integrated circuits is presented. A 6-bit digital phase shifter operating in the frequency range of 5-6 GHz was implemented on printed circuit board with commercially available surface mounted LC-components. FET based SPDT switches were used as controlling components. The phase shifter size is 27 mm × 16 mm. The phase shift error does not exceed 6°. A 360° analogue phase shifter was designed as a cascade of two transmission type 180° phase shifters each consisting of a 3-dB directional coupler and two identical reflection type phase shifters. Varactor diodes were used to provide the analogue control. The elements of the reflection type phase shifters as well as the 3-dB directional coupler were surface mounted onto a 0.5 mm thick alumina substrate. The dimensions of the phase shifter designed for the frequency range of 2.5-3.5 GHz are 8 mm × 6 mm. The insertion loss of the device is less than 2.5 dB.

I. Introduction

There are different technologies for microwave integrated circuits (MIC) production. Monolithic MIC technology allows realization of highly integrated devices though it is of high fabrication cost. Another drawback of this technology is a high level of insertion loss in the designed devices.

Hybrid technologies demonstrate devices with a moderate level of integration. In order to design miniature devices, the abundant multilayer hybrid technology (LTCC) is used. Another approach to design of hybrid MICs with surface mounted components makes it possible to organize mass production of low cost miniature devices exhibiting high performance.

This paper presents description of two microwave phase shifters based on surface mounted devices (SMD). The devices are designed in different ways: one phase shifter is a digital 6-bit phase shifter and another is an analogue phase shifter. The both devices have a compact size.

II. Design of 6-bit digital phase shifter

The 6-bit digital phase shifter was designed as a printed circuit board (PCB) with surface mounted components. Rogers RO3210 (h = 0.625 mm, ε_r = 10.2) was used as PCB material. High-Q chip inductors by Coilcraft and chip capacitors by ATC were used as SMD components. The 0402 chips have the miniature size of 0.6 mm × 0.3 mm. Switching was implemented by low loss FET single port double throw (SPDT) switches uPG2214TK by NEC.

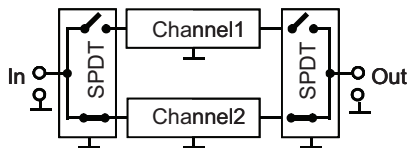The 45°, 90°, and 180° bits of the digital phase shifter were designed as

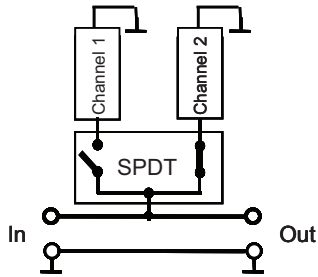**Fig. 1. Equivalent circuit of the switchable channels phase shifter (45°, 90°, and 180° bits).**

Fig. 2. Equivalent circuit of the smaller bits (5.625º, 11.25º, and 22.5º)

switchable channels (Fig. 1). Using traditional transmission lines with positive dispersion (right-handed transmission line – RHTL) in one channel and artificial transmission lines with negative dispersion (left-handed transmission line – LHTL) in another channel makes it possible to design broadband phase shifters with small phase shift error [1]. The RHTL section has negative value of the phase incursion while the LHTL section is characterized by positive phase incursion. In case of the same electrical length by absolute value at the central frequency, the phase characteristics of these transmission line sections have the same slope parameter that leads to a rather flat phase shift in a wide frequency band. The RHTL can be realized in two ways: as a distributed transmission line section or as an artificial one, whereas the LHTL can only be realized in the artificial way using T or Π-cells on lumped components.

The bits providing the phase shift of 5.625º, 11.25º, and 22.5º were realized by another equivalent circuit (Fig. 2) using only one SPDT switch. The phase shift is determined by the difference between electrical lengths of the channels.

The order of bits in the 6-bit phase shifter (Fig. 3) was optimized to provide a good input matching of the device in all states. Layout of the
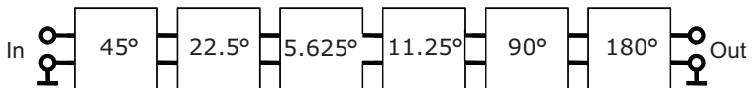

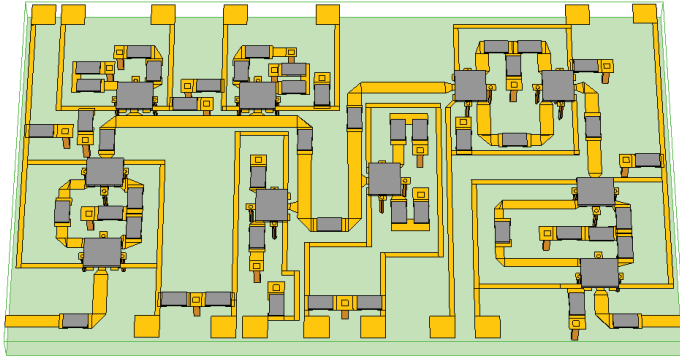**Fig. 3. The optimized order of bits of the 6-bit phase shifter.**

Fig. 4. The layout of 6-bit digital phase shifter with biasing networks.
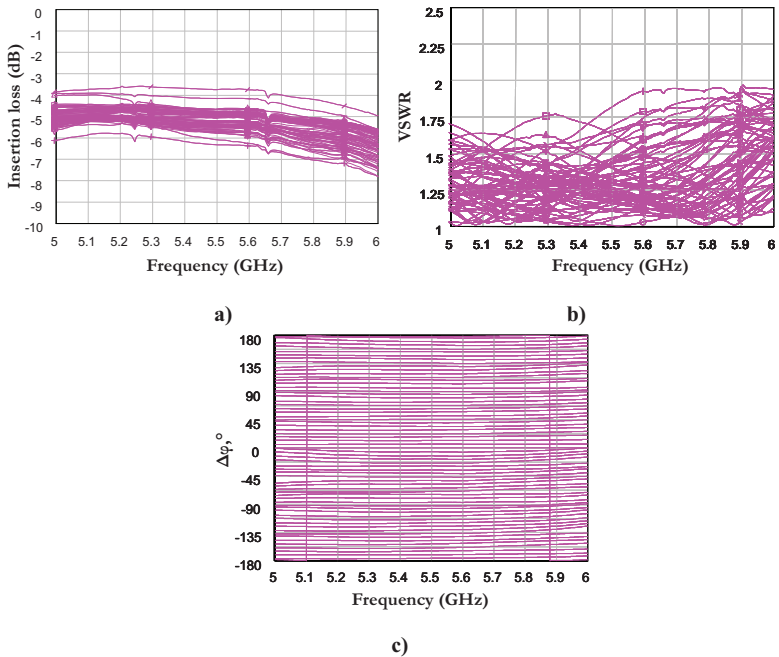

a)

b)

c)

Fig. 5. Experimentally obtained characteristics of the 6-bit digital phase shifter (a - insertion loss, b – VSWR, c – phase shift)
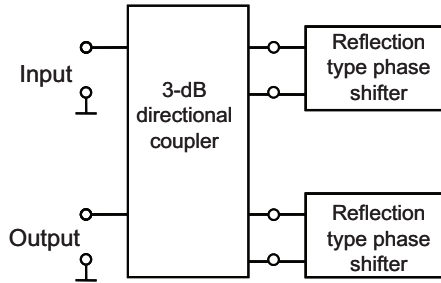
Fig. 6. Equivalent circuit of the 180° analogue phase shifter.

6-bit phase shifter is shown in Fig. 4. The size of the phase shifter is 27 mm × 16 mm.

The experimental characteristics of the device depicted in Fig. 5 show the phase shift of 0°-354.375° with the error less than 6° and the VSWR better than 2.0:1 in the frequency band of 5.0-6.0 GHz.

III. Design of 360° analogue phase shifter

The 360° analogue phase shifter for the frequency band 2.5-3.5 GHz was designed as a cascade of two 180° transmission type phase shifters each consisting of a 3-dB directional coupler with two identical reflection type phase shifters (Fig. 6). Each reflection type phase shifter consists of a controlling component connected with the output of the directional coupler through the impedance transforming network (Fig. 7). Analogue control is provided by the miniature flip-chip varactor diodes MV39003 by Microsemi, which are characterized by the commutation quality factor (CQF) [2] about 10,000 and a high tunability (n = C1/C2 = 20). In order to obtain the necessary value of the capacitance, two identical varactor diodes
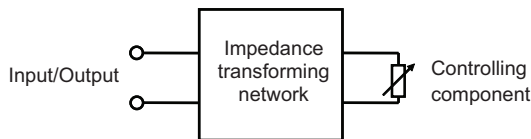

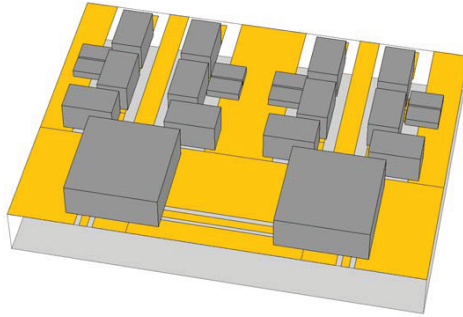**Fig. 7. Equivalent circuit of reflection type phase shifter.**

Fig. 8. Layout of the analogue phase shifter

were connected in shunt. All the elements of the phase shifter: the controlling components, the elements of the impedance transforming network as well as the integrated circuits of the 3-dB directional couplers were surface mounted on alumina substrate (Fig. 8). The area occupied by the phase shifter is 6 mm × 8 mm.

The impedance transforming network was designed taking into consideration the following conditions [3]: i) the reflection coefficient should be the same in two states $|\Gamma_1|^2 = |\Gamma_2|^2$ and ii) the phase shift should be equal to its nominal value at central frequency f_0 of the operational frequency band $\Delta\varphi = \Delta\varphi(f_0)$.

a)   b)
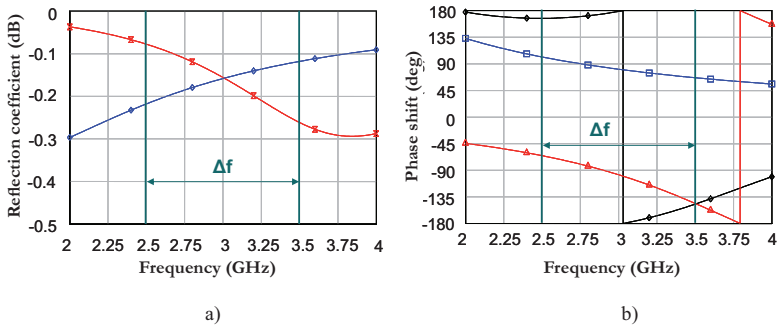
Fig. 9. Characteristics of the reflection-type phase shifter in two states corresponding to the minimum and maximum values of the varactor diode capacitance (a – reflection coefficient, b - phase shift).
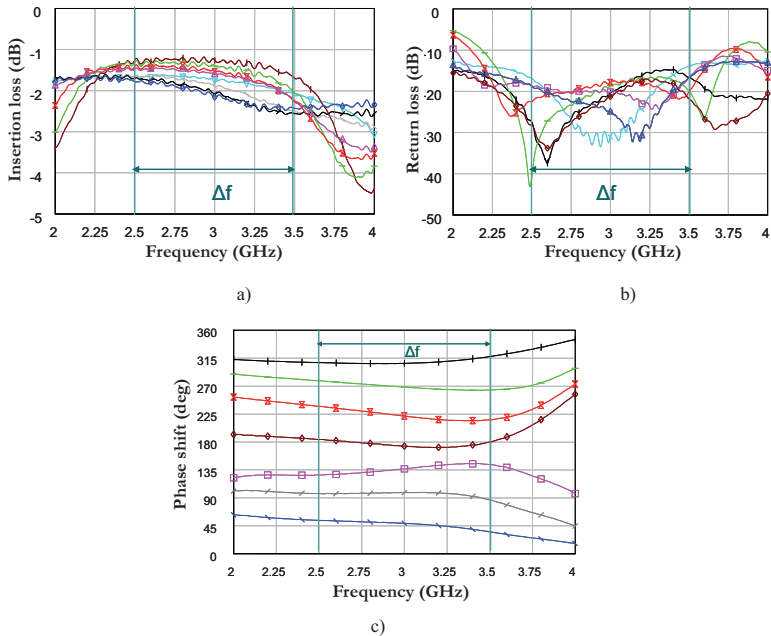
Fig. 10. Characteristics of the analogue phase shifter in eight states with the discrete of 45° (a - insertion loss, b - return loss, c – phase shift).

As the result the L-shape impedance transforming network consisting of a series inductance and a shunt capacitance was obtained. The characteristics of the reflection type phase shifter are depicted in Fig. 9.

In order to design a broadband phase shifter, the reflection type phase shifters as well as the 3-dB directional coupler should operate in the necessary frequency range. The miniature broadband 3-dB LTCC directional couplers [4] were used. The directional couplers have the size of 1.8 mm × 1.9 mm × 0.67 mm and exhibit the insertion loss less than 0.5 dB and the return loss better than 20 dB in the frequency range of 2.0 - 4.0 GHz.

The designed 360° phase shifter operates in the frequency band of 2.5 - 3.5 GHz. The device characteristics obtained by EM simulation are shown in Fig. 10. In the operational bandwidth, the insertion loss is less than 2.5 dB and the return loss is better than 13 dB.

IV. Conclusion

The designed phase shifters approve that the use of the hybrid integrated circuit technology with SMD components makes it possible to realize miniature microwave devices, which are low cost, easy reproducible, and of high reliability.

References

[1] I.B. Vendik, O.G. Vendik, D.V. Kholodnyak, E.V. Serebryakova, and P.V. Kapitanova, "Digital phase shifters based on right- and left-handed transmission lines", Proc. of European Microwave Association, Vol. 2, No. 2, pp. 30-37, March 2006.

[2] I. Vendik, O. Vendik, and E. Kollberg, „Criterion for a switching device as a basis of microwave switchable and tunable components", Proc. of 29th European Microwave Conf., 1999, Vol. 3, pp. 187-190.

[3] I. Vendik, O. Vendik, E. Kollberg and V. Sherman "Theory of Digital Phase Shifters Based on High-Tc Superconducting Films", IEEE Trans. On Microwave Theory and Techniques, august 1999, vol.47, No. 8

[4] P. Turalchuk, I. Munina, P. Kapitanova, D. Kholodnyak, D. Stoepel, S. Humbla, J. Muller, M.A. Hein and I. Vendik, „Broadband Small-Size LTCC Directional Couplers", Proc. of 40th European Microwave Conference, 2010, pp. 1162-1165.